Distinct functional roles and connectivity rules for lower- and higher-order intracortical and pulvinar thalamocortical pathways in mouse visual cortex

Xu Han[1,2,3], Vincent Bonin[1,2,4,5,6]

1 Neuro-Electronics Research Flanders, Kapeldreef 75, 3001 Leuven, Belgium.
2 KU Leuven, Department of Biology, 3000 Leuven, Belgium.
3 VIB-KU Leuven Center for Brain & Disease Research, 3000 Leuven, Belgium (current address).
4 VIB, 3001 Leuven, Belgium.
5 imec, 3001 Leuven, Belgium.
6 KU Leuven, Leuven Brain Institute, 3000 Leuven, Belgium.
Correspondence: xu.han@kuleuven.be; vincent.bonin@nerf.be

HIGHLIGHTS

- Similarly-tuned visual areas and pathways provide the strongest inputs to HVAs.
- Functional diversity within HVAs correlates with the diversity of cortical inputs.
- Higher-order L2/3 and LP thalamocortical pathways show high target specificity whereas higher-order L5 pathways lack this specificity.
- Tuning of higher-order pathways suggests prominent and specific contributions for these pathways to HVA representations.

SUMMARY

Functional specialization of cortical areas is a fundamental feature of brain organization and is critical for perception and behavior. Such an organization must depend on specialized connectivity between areas, yet the underlying wiring rules remain unclear. Using neural tracing and functional imaging, we characterized intracortical and thalamocortical pathways in the mouse visual cortex and uncovered multiple structural-functional connectivity rules underlying functional specialization of higher visual cortical areas (HVAs). Individual higher visual areas integrate specific cortical and thalamic inputs with distinct functional biases. Higher-order Layer 2/3 pathways and thalamocortical pathways show a higher degree of target specificity than feedforward intracortical pathways and might impart specific functional biases to the recipient HVAs; whereas higher-order Layer 5 pathways showing the least degree of specificity may contribute to the tuning diversity in the recipient HVAs. Altogether, this study revealed important organization rules of long-range interareal connectivity that underlie the parallel modular organization of the visual cortex.

INTRODUCTION

Functional specialization of cortical areas is a hallmark of the mammalian neocortex. In particular, the processing center of visual information, the visual cortex, features dozens of highly specialized higher-order visual cortical areas (HVAs) (Felleman and Van Essen, 1991), each encoding specific sets of visual features and involved in specific visual functions (Orban, 2008). For instance, the dorsal areas of the visual cortex are involved in visual motion processing and spatial behavior, whereas the ventral areas are specialized for color vision and object recognition (Hebart and Hesselmann, 2012; Priebe et al., 2003; Tanaka, 1996). These two groups of areas are often referred to as the dorsal and ventral processing streams (Goodale and Milner, 1992; Mishkin et al., 1983), and similar organizations of parallel cortical processing streams are also found across species, including the mouse (D'Souza et al., 2022; Han et al., 2022; Wang et al., 2012).

A diversity of long-range interareal pathways are suggested to contribute to visual processing streams (Gămănuţ and Shimaoka, 2021; Nassi and Callaway, 2009). Historically, feedforward intracortical pathways have been put forth as a major driver of HVA representations (Van Essen, 2005; Felleman and Van Essen, 1991). In primates, distinct subpopulations of V1 intratelencephalic (IT) neurons transit specific information to different compartments of V2, which then route parallel information to HVAs in the dorsal and ventral streams (Nassi and Callaway, 2009).

In mice, HVAs also show a high degree of specialization (Andermann et al., 2011; La Chioma et al., 2019; Han et al., 2022; Marshel et al., 2011; Murakami et al., 2017) and feedforward intracortical connectivity from V1 show functional tuning properties biased in the direction of the tuning properties of HVAs (i.e., target-specific) (Blot et al., 2021; Glickfeld et al., 2013; Kim et al., 2018; Murgas et al., 2020). However, silencing of V1 inputs only mildly impaired HVA visual representations (Tohmi et al., 2014), suggesting the necessity of additional input pathways. HVAs also receive inputs from other HVAs (Wang et al., 2012; Yao et al., 2022) and the lateral posterior thalamic nucleus (homologous to the pulvinar nucleus in the primates) (Bennett et al., 2019; Blot et al., 2021; Harris et al., 2019; Juavinett et al., 2020), which could contribute to HVA representations.

In mice, the number of presynaptic IT neurons in each source area can vary up to three orders of magnitude (Gămănuţ et al., 2018; Wang et al., 2012), suggesting different pathways have distinct contributions in interareal communication. At a finer resolution, interareal communication

pathways are composed of multiple 'lanes' that are mediated by distinct subtypes of IT neurons with distinct cortical laminar distributions and axonal projection profiles (Han et al., 2018; Harris et al., 2019). However, whether these parallel pathways mediated by distinct IT subpopulations are organized by similar rules and play similar functional roles, remains unclear.

The mouse lateral posterior thalamic nucleus (LP), the analogous structure of the primate pulvinar, is composed of multiple clusters of neurons that project to distinct HVAs (Bennett et al., 2019; Juavinett et al., 2020). In addition, different LP subregions show different responses to visual spatiotemporal frequencies and visual motion (Beltramo and Scanziani, 2019; Bennett et al., 2019; Blot et al., 2021), suggesting parallel pathways conveying different streams of spatiotemporal information from LP to different HVAs. However, the functional organization of these higher-order thalamocortical pathways remains to be systematically characterized.

In this study, we combined genetic circuit labeling with widefield microscopy and cellular imaging to characterize the joint anatomical and functional organization of input and output pathways to and from three HVAs, probing the visual tuning of lower and higher-order L2/3 and L5 intracortical pathways to areas AL, PM, and A, and of LP thalamocortical pathways to HVAs. At mesoscopic level, we found amongst intracortical pathways to the targeted areas, a tight correlation between the areas' response properties and the strength of long-range inputs. At cellular level, however, we found a diversity of intracortical connectivity patterns. While AL and PM integrate diverse visual inputs from diverse sources, area A receives much more homogeneous and stereotyped visual information. Furthermore, pathways to HVAs vary widely in their degree of target specificity with higher-order L2/3 pathways and LP pathways showing the highest degree of target specificity and higher-order L5 pathways showing the least degree of specificity. The properties of the pathways suggest higher-order HVA and LP pathways play prominent albeit specific roles in shaping functional diversity and specificity of HVAs.

RESULTS

Diverse excitatory neuronal populations underlie biased visual representations across HVAs

A diversity of neuronal pathways and functional response properties are suggested to underlie specialized representations and processing streams in the visual cortex (Gămănuţ and Shimaoka, 2021; Nassi and Callaway, 2009). In the mouse, higher visual cortical areas (HVAs) show specific spatiotemporal tuning properties (Andermann et al., 2011; Han et al., 2022; Marshel et al., 2011;

Murakami et al., 2017) and are innervated by specific pathways (Blot et al., 2021; Glickfeld et al., 2013; Han et al., 2018; Kim et al., 2018). To shed light on the joint functional and anatomical pathway organization giving rise to specialization, we characterized, using *in vivo* functional cellular imaging and neural circuit tracing, the spatiotemporal receptive field properties of intracortical and thalamocortical neurons projecting to and from specific HVAs (Figure 1A).

To get a comprehensive account of functional specialization in mouse visual areas, we characterized in TRE-GcaMP6s x CaMKII-tTA mice (N = 28 mice) (Wekselblatt et al., 2016) the spatiotemporal tuning preferences of >70,000 L2/3 excitatory neurons distributed across eight retinotopic visual areas. Previous studies of HVAs have shown tuning diversity both within and across visual areas (Andermann et al., 2011; Han et al., 2022; Marshel et al., 2011; Murakami et al., 2017; de Vries et al., 2020). These differences seem partially reflected in the input pathways (Blot et al., 2021; Glickfeld et al., 2013; Kim et al., 2018). To capture that diversity, we recorded in HVAs responses to three distinct types of visual stimuli sampling 30 combinations of spatial and temporal frequencies, two degrees of spatial anisotropy and four spatial orientations and directions of motion direction (Figure 1B, S1A-D) (see Star Methods). Visual areas were delineated using widefield calcium imaging (Figure 1B). V1, lateromedial (LM), anterolateral (AL), rostrolateral (RL), anterior (A), anteromedial (AM) and posteromedial (PM) (Wang and Burkhalter, 2007) were targeted with 2-photon (2P) recordings (Figure 1C). Cellular calcium responses were measured in the superficial cortical layer (L2/3, 100-300 um depths) and reliable visually tuned neurons were selected using correlational analysis (Figure S1F, cross-trial correlation > 0.3, see Star Methods).

The different types of stimuli yielded consistent tuning but evoked different response magnitudes (Figure S1A-D). For each neuron, we thus selected the measurements from the stimulus response set with the highest peak response magnitudes (Figure S1C, thick lines). Using 2-dimensional Gaussian function fits to the average calcium responses over stimulation epochs (Figure 1D, S1B-C), we computed the neurons' mean average response amplitudes, the preferred (peak) spatial and temporal frequencies, and the preferred (peak) speed (i.e., the particular spatial and temporal frequencies, and temporal-to-spatial frequency ratios eliciting the largest responses).

We first examined for each area the neurons' average response to the stimuli and observed widely distinct spatiotemporal tuning biases across visual areas (Figure 1E), consistent with recordings

in a different mouse line with GCaMP6 targeted to a subset of excitatory neurons (Han et al., 2022). While V1 shows the strongest activation for stimuli of low temporal frequencies, LM shows a peak at mid-range spatial and temporal frequencies and weak responses at high spatial frequencies, which is not seen in V1. In contrast, anterior visual areas (AL, RL, A and AM) are preferentially activated by stimuli of low spatial and high temporal frequencies (0.02-0.08 cpd, 4-16 Hz), whereas the posterior area PM shows a preference for low-temporal, high-spatial frequency stimuli (0.04-0.16 cpd, 1-4Hz). As visible in the pairwise correlation matrix of the neurons' average tuning maps, distinct tuning biases are observed in anterior and posterior HVAs (Figure 1F), suggesting HVAs may receive distinct visual information from different pathways.

We next examined the neurons' preferred spatiotemporal frequencies and observed a high diversity of tuning preferences in HVAs. Most areas differ in their distributions of peak spatial frequency, peak temporal frequency, and peak speed (Figure S1G) and these differences are robust to the correlation thresholds used to select visually-tuned neurons (Figure S1F). In many areas, the distributions of peak 2-dimensional spatiotemporal frequencies are separable with distinct modes at distinct spatiotemporal frequencies (Figure 1G). As observed for the average tuning, anterior and posterior HVAs show highly distinct spatiotemporal distributions (Figure 1 G, H). Within visual areas, neurons also show dispersed tuning preferences, as were observed in a majority of areas (V1, LM AL, AM, and PM). Although responses in A and RL appear less dispersed, the sample sizes for these areas were smaller. This high diversity suggests HVAs may receive diverse visual information from afferent pathways.

HVAs integrate specific visual inputs from functionally-similar visual areas

The tuning properties of HVA neurons suggest HVAs integrate specific and diverse visual inputs from other visual areas. To characterize multiway intracortical input pathways innervating HVAs, we performed injections of retrograde AAV (retroAAV-CAG-tdTomato) (Tervo et al., 2016) in GCaMP6 mice (Figure 2A-B). We targeted AL, PM and A which display distinct functional properties and receive distinct pathway innervation (D'Souza et al., 2022; Yao et al., 2022) and therefore should integrate distinct sets of inputs (Blot et al., 2021; Glickfeld et al., 2013; Kim et al., 2018). To characterize the magnitude of cortical inputs received from other visual areas, we captured in vivo widefield 1-photon (1P) fluorescence images of the cortical surface and examined tdTomato labeling patterns (Figure 2B-C). To estimate the magnitude of inputs from individual visual areas, we calculated the total fluorescence intensity over each non-injected area and

normalized the result to the highest values across non-injected areas (Figure 2D, normalized total fluorescence). 2P image stacks captured in vivo confirmed that this measure of connectivity correlates with the density of retrogradely-labeled somas (Figure S2).

These experiments revealed area-specific, functionally-related intracortical projection patterns to HVAs (Figure 2D-E). Consistent with previous anatomical work (D'Souza et al., 2022; Yao et al., 2022), HVAs receive inputs from distinct subsets of visual areas (Figure 2C-D). While AL and PM receive inputs from a broad set of visual cortical areas including V1, area A's intracortical innervation is more specific and largely restricted to anterior HVAs. Furthermore, the strength of innervation strongly depends on presynaptic area anatomical and functional identity. While AL and A receive their strongest inputs from anterior HVAs, PM receives its strongest inputs from posterior HVAs. Interestingly, the strength of intracortical connectivity and the similarity of functional tuning are correlated (Figure 2E), with AL, PM and A receiving their strongest innervation from similarly-tuned visual areas. Together, these data indicate HVAs receive specific intracortical inputs preferentially integrating information from similarly-tuned visual areas.

HVAs integrate non-random, specific visual inputs from both V1 and HVAs

Having observed a link between functional tuning and strength of intracortical connectivity, we next characterized the receptive field properties of intracortical neurons projecting to HVAs. Previous studies suggested specialized HVA representations result from the convergence of inputs from lower visual areas reporting in V1 and LM tuning biased towards the tuning of target HVAs (Blot et al., 2021; Glickfeld et al., 2013; Kim et al., 2018). To assess the distinct contributions of distinct pathways, including pathways from lower and higher visual areas, we characterized using 2P imaging in GCaMP6 mice the spatiotemporal visual tuning of V1 and HVA neurons projecting to AL, PM or A (Figure 3A-C, N=9, 13, 5 mice, respectively). We compared the tuning of tdTomato+ retrogradely-labeled neurons (tdT+) and non-labeled neurons (tdT–) in the area of origin and to the tuning of the populations in the target area. We asked whether the neurons show specialization, conveying diverse and specific visual information to HVAs. We considered two types of specificity: source specificity whereby neurons from different source areas convey distinct visual information to a specific target, and target specificity whereby projection neurons from the source area anatomically and functionally diverge showing tuning like that of their targets.

Comparing the tuning of projection neurons across areas of origin, we found HVAs receive both diverse and specific visual information from intracortical input pathways. The populations of

neurons projecting to AL and PM show diverse tuning, which varies by area of origin (Figure 3A-B, top). In comparison, A projecting neurons are more stereotyped, showing correlated tuning resembling the tuning of A neurons (Figure 3C, top). To quantify diversity amongst input pathways, we computed the distributions of pairwise tuning differences amongst populations of projection neurons, comparing the observed difference with that obtained for shuffled data (Figure 3A-C, bottom left) (see Star Methods). In a subset of projections, the tuning differences amongst neurons projecting to AL and PM deviate from that expected from shuffled data (Figure 3A-B, bottom left), indicative of heterogenous visual inputs from distinct visual areas. In comparison, neurons projecting to A did not show such a difference, indicative of more homogeneous visual inputs (Figure 3C, bottom left).

Despite their heterogeneity, the tuning properties of the pathways show an overall bias towards the tuning of their targets. This bias is visible in the multi-dimensional scaling of the matrix of pairwise correlation of average tuning (Figure 3D, S3C). To determine whether the similarity of tuning to the target area is due to specific connectivity or to the overall tuning bias in the source area, we compared using pairwise correlation analysis the tuning of intracortical projection neurons to the tuning of neurons in the target area (Figure 3A-C, bottom right; S3B, input pathways vs target areas, Cohen's d). We found that for the average tuning only a small subset of pathways shows target-specific connectivity, where the projection neurons differ from the non-labeled neurons showing higher tuning similarity to the target areas (e.g., Figure 3A bottom right, AL-proj vs non-AL-proj, Cohen's d). Amongst the input pathways to AL and PM, the reciprocal pathways between AL and PM are the most strongly target-specific (Figure 3A,B bottom right, AL-PM). The other input pathways to AL and PM show little indication of specificity using this metric. Intracortical pathways to A, in contrast, show more target specificity, with projections from V1, LM and PM showing significant average tuning specificity (Figure 3C, bottom right).

To study the population input patterns underlying specific connectivity, we examined the 2-dimensional distributions of peak spatial and temporal frequencies amongst retrogradely (tdT+) and non-labeled (tdT–) neurons in presynaptic visual areas. Similar distributions of peak spatiotemporal frequencies are an indication of random connectivity, whereas distinct distributions are evidence of specific connectivity. To compare distributions of spatiotemporal frequencies we used a two-sample two-dimensional Kolmogorov-Smirnov test (2d-KS test).

The analysis of peak spatiotemporal frequencies yielded similar results whereby V1 and LM pathways to AL and A and reciprocal pathways between AL and PM show strong specificity, whereas other pathways show comparatively less specificity (Figure 4, S4). Thus, intracortical pathways provide diverse information to HVAs and vary widely in their degree of specificity. Some of the diversity of inputs to HVAs is imputable to target specific projections while others reflect a functional bias in the area of origin. Interestingly, amongst all intracortical pathways that were probed, bidirectional AL – PM pathways appear to show the highest degree of specificity.

L5 HVA neurons show weak target specificity and broadcast stereotyped visual information to lower and higher visual areas

While HVA neurons in L2/3 can send specific visual information to other HVAs, it is unclear whether the specificity of HVA pathways extends to neurons in other cortical layers. L5 neurons project intracortically and subcortically and hence could abide by distinct connectivity rules (Kim et al., 2015; Lur et al., 2016), however, L5 neurons in V1 were shown to display target specificity (Glickfeld et al., 2013). To examine the specificity of L5 HVA neurons, we used multiplane 2P imaging in retroAAV-CAG-tdTomato injected GCaMP6 mice to image the spatiotemporal visual tuning of AL and PM neurons in L2/3 and L5 (Figure 5A-D, ~200-500 um deep, 6 mice for AL→PM pathway, 5 mice for PM→AL pathway). The 2P imaging yielded robust neuronal tuning in both L2/3 and L5 neurons (Figure S5A). We therefore compared the tuning of tdT+ and tdT L2/3 and L5 neurons in the source areas to the tuning of neurons in the target areas.

The experiments revealed weak tuning specificity in L5 HVA projection neurons. HVA L2/3 and L5 neurons show similar tuning biases in L5 as in L2/3 (Figure 5E, tdT–, L2/3 vs L5; Figure S5B). As for L2/3 neurons, L5 neurons in AL prefer low spatial and high temporal frequencies and L5 PM neurons have the opposite bias, preferring high spatial and low temporal frequencies (Figure 5E; S5B-C). However, unlike L2/3 HVA-to-HVA projection neurons, which show specific tuning preferences aligned to those of their target (Figure 5E-F, L2/3 tdT+), L5 HVA-to-HVA projection neurons show more unspecific tuning matching that of the general unlabeled population (Figure 5E-F, L5 tdT+). Specifically, while L2/3 tdT+ PM neurons show a pronounced spatiotemporal tuning shift towards the preferences of AL, L5 PM tdT+ neurons do not. Likewise, the shift shown by L2/3 AL tdT+ neurons towards the PM-like preferences is not observed for L5 AL tdT+ neurons. Thus, while AL and PM L5 neurons show functional specialization, L5 AL and PM pathways do not show the target specificity that is observed in L2/3.

To determine whether weak specificity is restricted to AL and PM pathways or a general characteristic of HVA L5 pathways, we looked at the visual information conveyed by the axonal projections of L5 neurons in area AL or PM across multiple visual cortical areas (Figure 6A). To selectively label L5 neurons, we injected in transgenic mice with Cre-expressing L5 neurons (Rbp4-Cre mouse line, 4 mice for AL injection, 4 mice for PM injection) AAV that induces Cre-dependent expression of GCaMP8 (AAV-CAG-Flex-GcaMP8m) (Zhang et al., 2023)(Figure 6B). We then used 2P imaging to measure the spatiotemporal tuning of the transfected L5 neurons in AL or PM, as well as the tuning of their axonal projections in the superficial layers (~20-150 um deep) of distant cortical areas (Figure 6B-C). In this Cre driver line, L5 V1 neurons were shown to display target specificity (Glickfeld et al., 2013). While functionally tuned axons from AL L5 neurons were observed in V1 and all dorsal HVAs, axons from PM L5 neurons to areas RL and A were too sparse to be examined. Putative axonal boutons, the 'hot spots' on the axons with high calcium fluorescence fluctuations, were identified (Figure 6C). Stimulus-evoked responses of axonal boutons were used to estimate the spatiotemporal tuning parameters as described above for the cellular datasets (Figure 6D).

Examining the tuning of axonal projections from these areas, we observed that the labeled L5 neurons broadcast highly stereotyped visual information to other visual cortical areas (Figure 6E). Similar to the cellular data measured in L5 of TRE-GCaMP6s x CaMKII-tTA mice (Figure 5), GCaMP8 labeled L5 neurons in AL and PM show opposite spatiotemporal tuning preferences (Figure 6E, left). However, in all areas, the tuning of axons matches that of neurons in the source areas (Figure 6F, L5 axon vs L5 neurons), which is not necessarily the case for the target areas (Figure 6F, L5 axon vs target). Therefore, unlike L2/3 pathways which are functionally target-specific, L5 pathways broadcast similar visual information to recipient areas, potentially contributing to functional diversity in those areas.

This observation in the spatiotemporal tuning properties of L5 neuron subsets is quite distinct from that observed when imaging axonal projections labeled by non-layer-specific viral injection (AAV2/1.Syn.GCaMP6f.WPRE.SV40 in AL or PM of C57BL mice) (Figure S6). When looking at the functional specificity of overall axonal outputs from neurons across layers (including both L2/3 and L5) in area AL or PM, we found that both AL and PM (especially AL) outputs are more diverse compared to L5 outputs alone (Figure S6D-G).

LP pathways carry highly specific, highly diverse visual information to HVAs

The tuning properties of intracortical pathways, although specific, cannot easily explain the functional biases of HVAs (e.g., tuning for low SF and high TF in AL, Figure 1G). Overall, the biases in spatial, temporal, and speed preferences are relatively minor compared to the preferences of HVAs (Figure S7A). We hypothesized that LP inputs, with their high specific anatomical connectivity (Beltramo and Scanziani, 2019; Bennett et al., 2019; Juavinett et al., 2020), impart specific visual information to HVAs and drive area-specific functional biases.

To investigate this hypothesis, we characterized the visual tuning of LP axonal projections innervating V1 and HVAs (Figure 7A). Using stereotaxic injections of AAV2.1-hSyn-GCaMP6f viral vector in naïve C57/BL mice (5 mice), we induced GCaMP6 expression in LP neurons and their axonal arborizations (Figure 7B; Figure S7B). Using 2P imaging in V1 and HVAs, we recorded LP axons' responses to visual stimuli of different spatial and temporal frequencies and characterized the tuning of responses. Labeled LP axons were found in V1 and subsets of HVAs. We focused on axonal boutons in the superficial cortex (~20-150 μm from the pia).

The axonal projections from LP to different HVAs show distinct spatiotemporal tuning (Figure 7C, peak SFTF; 7D, population tuning maps). Whereas the LP→AL pathway shows responses tuned to low spatial and high temporal frequencies, the LP→PM pathway is selective for high spatial and low temporal frequencies. These two pathways encode almost non-overlapping ranges of preferred frequencies. Such functional segregation is observed across higher-order thalamocortical pathways, where the LP projections targeting different higher visual areas exhibit widely different spatiotemporal selectivity (Figure 7C-D, S7C).

Furthermore, the tuning of LP axons in HVAs matches the tuning preferences of the target HVAs (Figure 7E, matched vs shuffled, Cohen's d), showing pronounced target-specificity. In comparison, LP axons in V1 do not show such a match (Figure 7E, V1), with LP to V1 projections showing functional tuning biases distinct from those of V1 neurons (Figure 7C,D, LP->V1; compare to V1 in Figure 1E). While projections from LP to HVAs and V1 are considered feedforward and feedback pathways respectively (Miller-Hansen and Sherman, 2022), LP pathways might therefore contribute differently to the visual representation and visual processing in HVAs and V1 with inputs of distinct specificity.

Finally, while L2/3 intracortical and LP pathways carry target-specific information to HVAs, they differ in the degree of specificity and might differently shape the visual representations in HVAs.

The input pathways showing a higher degree of specificity might drive the biases of visual representations, while less specific but diverse inputs may contribute to the diversity of visual representation. Comparing the target specificity across major input pathways to AL and PM, we found LP pathways are remarkably more functionally aligned to the target areas than the L2/3 input pathways from V1 and LM (Figure 7F), suggesting a primary role of higher-order thalamocortical pathways in the formation of specialized visual representations in HVAs.

DISCUSSION

In this study, we characterized the functional organization of lower and higher-order L2/3 and L5 intracortical pathways to AL, PM and A, and of LP thalamocortical pathways to HVAs. At the mesoscopic level, we found between intracortical pathways to targeted areas, a tight correlation between the neurons' response properties and the anatomical strength of long-range intracortical inputs. At the cellular level, however, we found a diversity of intracortical connectivity patterns. While AL and PM integrate diverse visual inputs from diverse sources, area A receives much more homogeneous and stereotyped visual information. Furthermore, pathways to HVAs vary widely in their degree of target specificity with higher-order L2/3 pathways and LP pathways showing the highest degree of target specificity and higher-order L5 pathways showing the least degree of specificity. The properties of the pathways suggest higher-order HVA pathways and LP pathways play a prominent role in the diversity and specificity of HVA representations.

Roles of cortical and thalamic input pathways in visual representations of HVAs

Our data show feedforward intracortical pathways are functionally target-specific but may only play a limited role in establishing specialized visual representations in HVAs. L2/3 neurons projecting from V1 to areas AL or PM show relatively weak target-specificity, consistent with previous studies (Glickfeld et al., 2013; Kim et al., 2018). Projections from LM to AL or PM also present modest functional target-specificity, in line with previous observations (Glickfeld et al., 2013). However, these feedforward pathways alone cannot easily explain functional biases in AL and PM (Figure S7A). For area A, although the input from V1 and LM are highly specific (Figure 3), they are too sparse to be the main source of information (Figure 2). Therefore, our data contradict the view of feedforward intracortical pathways as the driving force of specialized visual representations in HVAs and call for the consideration of higher-order pathways.

Our data show the specific organization of L2/3 higher-order intracortical pathways, which carry biased yet diverse information and might contribute to different components of visual

representation in the recipient areas (Figure 3-4). Target-specificity is particularly evident in the pathways to area A, where projection neurons in HVAs all show stereotyped tuning aligned to neurons in area A (Figure 3). Anterior dorsal areas (AL, RL, and AM) particularly provide dense inputs to area A (Figure 2C,D), suggesting important contributions to area A. In contrast to this mode of stereotyped inputs, area AL receives biased but diverse inputs across HVAs (Figure 4). The projections from area PM likely contribute to the response to low temporal frequencies, while projections from anterior areas might contribute to the response to high temporal frequencies (Figure 3A). Similarly, for area PM, inputs from AL or AM might impart different information to distinct neuron subpopulations in PM (Figure 4B). Since this study was focused on dorsal visual cortical areas, it will be important to examine the structural-functional organization of L2/3 higher-order pathways amongst ventral areas and between dorsal-ventral processing streams (Gămănuţ et al., 2018; Wang et al., 2012) and explore their roles in visual processing.

L5 higher-order intracortical pathways, in contrast to L2/3 pathways, broadcast source-specific information across cortical areas (Figure 5, 6). How this information is integrated into the recipient areas is unclear. In a 'segregated channels' model, L5 neurons preferentially innervate neurons that show similar tuning properties (i.e., same visual processing channels) in the target areas, forming long-range interareal functional subnetworks. This model predicts that areas with essentially no common functional cell types should avoid interconnecting. It is supported by the observation that functionally distinct areas, PM and A, have very sparse reciprocal connections (Figure 2). In an 'integrated channels' model, L5 intracortical pathways innervate neurons with different visual tuning properties, allowing information integration (between visual processing channels) and 'de novo' generation of complex feature selectivity. Alternatively, L5 pathways may recruit inhibitory circuits in the recipient areas, which might in turn enhance the selectivity for the opposite visual features via a 'push and pull' mechanism. These possible mechanisms may coexist and synergistically shape higher-order visual representations. Future studies dissecting the postsynaptic circuitries are necessary to understand the wiring principles and functional impacts of L5 intracortical pathways.

Higher-order thalamocortical pathways from LP to HVAs show distinct visual tuning and remarkable functional target-specificity, suggesting parallel segregated visual streams that may impart different functional biases to different HVAs (Figure 7). While a recent study reported mixed degrees of specificity in two LP pathways projecting to AL and PM (Blot et al., 2021), our data,

which covered the LP pathways to most dorsal HVAs, show universal high target-specificity (Figure 7E). Critically, the specificity is lower for LP projections to V1 than projections to HVAs (Figure 7E), suggesting high target-specificity is specific to feedforward thalamocortical pathways. While it becomes clear that different LP neurons convey specific visual information to distinct HVAs via highly specific anatomical projections (Bennett et al., 2019; Juavinett et al., 2020), it is unclear which input pathways impart LP high specific spatiotemporal tuning properties. LP receives visual information mainly from SC and the visual cortex. From SC, widefield neurons, which are selective for high-spatial and low-temporal frequencies (Gale and Murphy, 2014), preferentially target the posterior LP that connects to ventral HVAs (Beltramo and Scanziani, 2019; Bennett et al., 2019). Hence SC is unlikely the source of high temporal frequency information that prevails anterior dorsal HVAs (Figure 1E). From the visual cortex, both feedforward (V1→LP) and feedback (HVA→LP) pathways were reported to contribute to LP overall activities (Bennett et al., 2019; Blot et al., 2021). It is possible that LP subpopulations inherit specific visual selectivity from V1 corticofugal neurons, which get amplified through the reciprocal LP--HVA connections (Bennett et al., 2019). This possibility remains to be tested. In addition, the prefrontal cortex may exert 'top-down' modulation of visual tuning of LP neurons via direct or indirect pathways (Bennett et al., 2019; Hu et al., 2019) and facilitate feature-specific visual processing and behavior (e.g., feature-based attention). Taken together, future studies are necessary to elucidate the input-output connectivity and function of LP in bottom-up and top-down visual functions.

Distributed and segregated cortical subnetworks

Our results of intracortical connectivity also suggest distributed cortical subnetworks consisting of functionally alike neurons that are interconnected within and across cortical areas. Within each area, neurons with similar projection patterns and/or visual tuning properties are more likely to interconnect (Cossell et al., 2015; Kim et al., 2018; Ko et al., 2011; Lee et al., 2016). Diverse intracortical projection cell types with distinct projection targets and/or spatiotemporal visual tuning (Figure 4)(Han et al., 2022, 2018; Kim et al., 2020) hence may form multiple segregated local subnetworks that process and transmit specific spatiotemporal information to different visual areas. Across areas, functionally-alike neurons in different areas might form distributed interareal subnetworks via recurrent long-range connections. Such organization is suggested present between mouse V1 and HVAs. While V1 neurons send target-specific information to area AL (Glickfeld et al., 2013; Kim et al., 2018), AL in turn preferentially targets V1 neurons with AL-like tuning (Huh et al., 2018). Similar reciprocal connections are also found between V1 and PM (Huh

et al., 2018) and might exist amongst HVAs. Moreover, local subnetworks in different areas can be interconnected via the collateral axonal projections of intracortical cells (Han et al., 2018). Such recurrent subnetworks might permit signal amplification and prolonged information integration windows (Li et al., 2013a, 2013b; Lien and Scanziani, 2013). Future studies are necessary to determine whether neurons in different cortical areas form monosynaptic, reciprocal loops, and determine the interaction between functional subnetworks within and between cortical areas.

Our data also suggest different HVAs differentially partake in distributed cortical subnetworks. Areas PM and A encode essentially nonoverlapping visual information and partake in separate subnetworks as they avoid connecting with each other (Figure 2) and receive segregated inputs from distinct subsets of areas, and from distinct subpopulations in the common source areas (e.g. AL→ PM and AL→A; Figure 3,4). Such anatomical segregation constrains the information exchange between the two areas and supports function segregation. Area A might be especially involved in a multi-area subnetwork in the dorsal cortex for processing fast visual motion. It receives profound inputs from adjacent anterior dorsal areas, which also show strong preferences to fast motion (Han et al., 2022). These short, dense connections between anterior areas may provide a neural substrate for fast transmission of information about fast visual motion and may support the proposed roles of these areas in animals' exploratory behaviors (La Chioma et al., 2019; Zhuang et al., 2017). In the meantime, area AL may participate in multiple distributed subnetworks with diverse AL subpopulations connecting to distinct neuronal populations or distinct areas.

Relationship between projection neurons cell type and visual tuning

Our data demonstrated L2/3 and L5 intracortical projection neurons convey distinct information between higher visual areas, suggesting parallel pathways mediated by distinct cell types. Rbp4+ L5 neurons are composed of three broad transcriptional subtypes with distinct laminal positions and projection targets (Munz et al., 2023). The L5a subtype mainly projects intracortically and may be the main source of the axons we imaged in distal HVAs (Figure 6). These Rbp4+ L5a intracortical projection cells in AL and PM broadcast source-specific information across visual cortical areas, suggesting a potential link between the neuron's transcriptional identity and functional property. Interestingly, several subtypes of intracortical projection neurons, expressing a diversity of molecular markers, have recently been identified (Tasic et al., 2018). Each shows distinct axonal termination patterns in the target cortical areas (Harris et al., 2019). Further

divisions of these populations are highly likely since the reciprocal connections between two areas mediated by neurons expressing the same molecular marker often target different layers (Harris et al., 2019). These subtypes might follow distinct wiring rules and send distinct information. Ultimately, multi-dimensional surveys, combining in vivo physiology, anatomy with single-cell transcriptomic profiling of long-range projection neurons, will lead to a better understanding of the genetic and functional logic of long-range connectivity in the cortex.

Conclusions

Overall, this study provides a detailed characterization of the anatomical and functional organization of the input and output of higher visual cortical areas, and uncovered cell-type and area-specific logic of intracortical and thalamocortical pathways. Highly specific pathways (e.g., higher-order thalamocortical pathways, L2/3 pathway to area A) can impart functional biases to HVAs, whereas less specific inputs (e.g., L2/3 and L5 intracortical pathways to AL and PM) conveys diverse information and can contribute to the richness of visual representations in HVAs.

STAR METHODS

EXPERIMENTAL MODEL AND SUBJECT DETAILS

Mice

All experiments were approved by the Animal Ethics Committee of KU Leuven. Three mice genotypes were used: naïve C57BL/6 mice, Rbp4-Cre mice [Tg(Rbp4-cre)KL100Gsat, MGI:4367067] (Harris et al., 2019), and CaMKII-GCaMP6 mice [B6;DBA-Tg(tetO-GCaMP6s)2Niell/J x B6.Cg-Tg(Camk2a-tTA)1Mmay/DboJ; The Jackson Laboratory stock No. 024742 and 007004] (Wekselblatt et al., 2016). The mice were single-housed in an enriched environment (cotton bedding, wooden blocks, and running wheel), with 12h-12h light-dark cycle, 19–21 degrees cage temperature, 30–70% humidity.

Craniotomy

Standard craniotomy surgeries were performed to gain optical access to the visual cortex (Goldey and Andermann, 2014). Mice between 2 and 3-month-old were anesthetized with isoflurane (2.5%–3% induction, 1%–1.25% surgery). A custom-made titanium frame was attached to the skull, and a glass cranial window was implanted in the left hemisphere over the visual cortex. In five mice, a 5-mm cranial window was centered over V1 (3.10 mm lateral from lambda, 1.64 mm anterior of the lambdoid suture). Buprenex and Cefazolin were administered postoperatively when

the animal recovered from anesthesia after surgery (2 mg/kg and 5 mg/kg respectively; every 12 hours for 2 days). All mice were habituated at least 3 days before data acquisition.

Viral injection

Labeling of long-range connectivity was achieved by injecting anterograde or retrograde neural tracers into the cortex or LP of anesthetized mice. Anesthesia and post-operative treatments were delivered as described in the above section. To precisely target specific HVAs, visual cortical areas are first identified using retinotopic mapping, using widefield calcium imaging on GCaMP6 reporter mice, and widefield flavo imaging in non-GCaMP6 mice (see details below, Retinotopic mapping). In a typical viral injection, a glass injection capillary (~15-25 μm internal tip diameter) was first loaded with the viral vector, and then the capillary tip was slowly lowered to the desired coordinates. After 10 min of recovery, viral vectors were slowly pulse-injected (25nl per min, Nanoject II, Drummond Sci.), followed by 10 min recovery before the capillary was slowly retracted from the brain. To induce specific expression of GCaMP in L5 neurons, Cre-dependent adeno-associated virus constructs (AAV1-CAG-FLEX-jGCaMP8m-WPRE, addgene 162381-AAV1) (Zhang et al., 2023) were injected into selected areas (AL or PM, 50nl at 500 um depth) of Rbp4-Cre mice. To induce expression of GCaMP in excitatory neurons across cortical layers, AAV constructs (AAV2/1.Syn.GCaMP6f.WPRE.SV40; University of Pennsylvania Vector Core) were injected into selected areas (AL or PM, 50nl each at 500 and 200um depths) in naïve C57BL6 mice. To label intracortical projection neurons projecting to selected cortical areas, retrograde AAV constructs (retroAAV-CAG-tdTomato, addgene 59462-AAVrg) (Tervo et al., 2016) were injected into selected areas (AL, PM or A, 20nl each at 200 and 500 um depths) of CaMKII-GCaMP6 mice. To label LP neurons with GCaMP, anterograde AAV constructs (AAV1.CAG.GCaMP6f.WPRE.SV40, addgene: 100836-AAV1) were injected into LP (1.90 mm posterior, 1.70 lateral from bregma, at the depth 2.50 mm) in C57BL6 mice. For inspection of the expression, images were taken using 1-photon and 2-photon imaging (see the following sections). The tdTomato expression increases over time and becomes clearly visible one week after injection. GCaMP6 expression in cell bodies and axons was visible three weeks after injection of AAV constructs with a Syn promotor, and two weeks for AAV constructs with a CAG promotor.

Histology

For histology, mice were perfused with 25 ml 0.1mM PBS and then 25 ml of 4% paraformaldehyde (PFA, Invitrogen). The whole brain was extracted and stored overnight in 4% PFA. A series of

coronal or sagittal sections (100um thick) were obtained using a Lieca VT100S vibrosector and stored in PBS with 0.5 mg/mL sodium azide (Sigma). An immunostaining process was performed to enhance the signal of GCaMP6 of axons. Slices were blocked with PBS supplemented with 3% donkey serum (Invitrogen) and 0.3% Triton X-100 (Sigma) for 1 h, and incubated overnight at 4 °C with the primary antibody (1:1000 anti-chicken, polyclonal, Thermo Fisher Scientific). Slices were rinsed with PBS/0.1% Triton X-100 three times and then incubated 2 h at room temperature with the secondary antibodies (1:800 Alexa 488 donkey anti-chicken, Immuno-Jackson). Sections were again rinsed three times with PBS/0.1% Triton X-100 and then twice in PBS. The sections were next mounted on a Superfrost slide (Thermo Scientific) and dried using a brush before adding histology mounting medium with DAPI (Fluoroshield with DAPI, Merck). Confocal images were acquired using a Zeiss LSM710 confocal microscope controlled by the Zen Black software (Zeiss).

Visual stimulation

Visual stimulation was performed as previously reported (Han et al., 2022). A 22-inch LCD monitor (Samsung 2233RZ, 1680 by 1050-pixel resolution, 60 Hz refresh rate, brightness 100%, contrast 70%) with a mean luminance of 54–80 cd/m^2 (from edges to center) was positioned 18 cm in front of the right eye, covering 100 by 80 degrees of the visual field (0 to 100 deg in azimuth from central to peripheral and -30 to 50 deg in elevation from lower to upper visual field). Visual stimuli were generated in MATLAB (The Mathworks, Natick, MA) and presented using PsychoPy2 and custom Python code. A spherical geometric correction was applied to the stimuli to define eccentricity in spherical coordinates.

To activate cortical neurons with diverse tuning for orientation features and visual motions (Han et al., 2022; Niell and Stryker, 2008), three sets of visual stimuli were used: isotropic noise stimuli (ISO) containing non-oriented textures, anisotropic noise stimuli (ANISO) containing elongated textures, and drifting gratings. The ISO and ANISO stimuli were generated by applying a set of parametrized filters to random pink-noise fields, as described before (Han et al., 2022). Narrow bandpass filters (bandwidth: 1 octave) for spatial and temporal frequencies determine the scale and flickering frequencies of the textures. The orientation bandwidth determines the length/width ratio of the textures. Isotropic noise stimuli, which are spectrally band-passed noise with no angular filter, resemble clouds of moving dots (Figure S1A, ISO stimuli icons). A narrow orientation bandwidth (15 deg) creates elongated textures (Figure S1A, ANISO stimuli icons).

While isotropic textures contain no global motion, oriented textures were designed to slowly rotate (45 deg per second, clockwise) to activate neurons tuned to different orientations. The drifting gratings (Figure S1A, gratings icons) differ from the noise stimuli as they contain coherent visual motion, a key component to active specific neuronal populations (Sit and Goard, 2020). For the drifting gratings, each spatiotemporal frequency combination was presented as gratings moving in four cardinal directions (up, down, nasal, temporal, 1s for each direction, no blank in between).

To probe the neuron's selectivity for spatial and temporal frequencies, the three visual stimulus sets, each consisting of 30 combinations of spatial frequencies (0.02, 0.04, 0.08, 0.16, 0.32 cpd) and temporal frequencies (0.5, 1, 2, 4,8,16 Hz), were displayed to the mouse. Each frequency combination was presented for 4 seconds, intertwined with 4-second equiluminant gray screen. All combinations were presented in random orders, for 4 repeats. In each repeat, a unique set of ISO and ANISO noise stimuli was generated by using distinct random seeds.

Cortical neurons showed differential preferences for isotropic, anisotropic noise, and moving grating stimuli. In all L2/3 neurons detected across areas, 41% of neurons showed reliable stimulus-evoked responses to at least one stimulus set (75th percentile cross-trial correlation > 0.3). The three stimulus sets activated overlapping yet distinct populations of neurons (Figure S1G). Gratings showed the best capability to drive neuronal responses in terms of the fraction of activated neurons and response amplitudes (Figure S1D,E). The stimuli driving the strongest responses were deemed a neuron's preferred stimuli and the corresponding responses were used for spatiotemporal tuning analysis (see below, Tuning analysis).

Two-photon functional and structural imaging

For 2-photon imaging, a 920-nm femtosecond laser beam (Newport MaiTai DeepSee) was raster-scanned using galvo and resonant scanners (Cambridge 6215H and CRS 8K). With 16x lens (NA = 0.8, Nikon), activity from neurons was recorded typically at 100~300 μm deep below pia for L2/3 neurons, 350~500 μm deep for L5 neurons, 200~500 μm deep for simultaneous imaging of L2/3 and L5 neurons. Activity from axonal projections was recorded typically at 20~150μm deep with 2x digital magnification. GCaMP6 fluorescence was collected using a bandpass filter (510/84 nm, Semrock) and GaAsP hybrid photodetectors (H11706-40, Hamamatsu), and images were reconstructed and acquired using Scanbox (version 4.0, https://scanbox.org). Individual imaging planes (720x512 pixel per frame, 1249 by 1067 um field-of-view) were collected at different depths. Simultaneous multi-plane imaging was achieved by rapidly changing the focus with an

electrically tunable lens (EL-10-30-TC, Optotune AG; staircase mode) from 100 to 300 um depth and varying the laser power (from ~50 to 120 mW). Images were acquired from 3 or 4 evenly spaced planes at rates of 10.33 and 7.75 Hz, respectively. Blackout material (Thorlabs) blocked stray light from the visual display entering the collection light path.

High-resolution structural image stacks of retrogradely labeled cells in the cortex were obtained with the collection of two-photon cellular images every 5 um (controlled by motorized stages, averaged over 50 frames per section) from the pia to 500 um depth in the cortex. Red fluorescence of tdTomato was collected using a bandpass filter (607±35 nm, Semrock).

Widefield fluorescent Imaging

Widefield calcium and flavo imaging was conducted using a widefield in vivo microscope (Neurolabware LLC), performed with blue excitation light (479nm LED, 469/35 nm bandpass filter, Thorlabs) through a low magnification (2x) objective lens (NA = 0.055, Mitutoyo) and green emission light (498 nm dichroic, 525/39 nm filter, Semrock) collected with an EMCCD camera (QImaging EM-C2, Teledyne Photometrics; 1,004 by 1,002 pixels with 2 by 2 binning) at a rate of 5 frames per second (fps).

Widefield retrograde labeling imaging was performed with a fluorescent microscope with 1x objective. A green light beam from a halogen lamp passing through an excitation filter was used for illumination. The red fluorescence was collected with a CCD camera (pco.pixelfly 1.3 SWIR) and acquisition software (pco.camware). The acquired images were filtered with a bandpass kernel using ImageJ.

Retinotopic Mapping

Visual cortical areas were identified using retinotopic mapping as previously described (Han et al., 2022). We use dynamic noise stimuli partially visible through a circling round window ("circling patch") or a translating rectangular band ("traveling bar"). The circling patch stimuli is a small patch of isotropic noise stimuli (0.08 cpd, 2 Hz, 20 deg in diameter) circling along an elliptic trajectory on the display (azimuth: 10 to 90 deg; elevation: -20 to 40 deg; 20 sec per cycle with 20 repetitions). The traveling bar stimuli comprised a narrow band (13 deg wide) of isotropic noise stimuli (0.08cpd, 2Hz) sweeping across the screen in 4 cardinal directions (10 sec per sweep, 20 repetitions). The phase maps were generated by calculating the phase/position of the stimuli evoking maximal neural responses for each image pixel. Each area has a complete

representation of the elliptic trajectory of the circling patch, resulting pinwheel-like retinotopic maps. The traveling bar stimuli generated azimuth and altitude phase maps, which were used to identify the reversals of retinotopic maps between areas. Areas are identified according to the common delineation (Wang and Burkhalter, 2007; Zhuang et al., 2017).

Data Analysis

All subsequent data analysis was performed in MATLAB (The Mathworks, Natick, MA).

Anatomical connectivity analysis

To determine the degree to which widefield fluorescence intensity of retrograde labeling (tdTomato) reflects the amount of labeled neurons, we measured the density of labeled populations using 2-photon structural imaging (from pia to ~ 500um deep) and found a high correlation between the two measurements (Figure S2). Regions of high fluorescent intensity contain dense retrograde labeling of projection neurons, distributed in superficial and deep layers, whereas low-intensity regions contain much sparser labeled neurons (Figure S2C). The average intensities of one-photon images and corresponding two-photon volumes were highly correlated (Figure S2D-E), permitting the use of the total fluorescent intensity of each cortical area as a metric of the total number of retrogradely labeled neurons.

To determine the relative strengths of intracortical input pathways to a given HVA, we calculated, from the widefield fluorescent images, the total fluorescent intensity (sum of all pixels) of retrograde labeling of individual visual cortical areas (I_x) that were identified using retinotopic mapping. The anatomical connectivity strength of pathway x is calculated as:

$$W_x = I_x / \max\{ I_x, x = 1{:}n\},$$

Where n is the total number of retrogradely labeled areas.

Cellular and axonal calcium imaging data.

Imaging processing and analysis were described in our previous study (Han et al., 2022). To correct x-y motion, 2P images for all experiments during the imaging sessions were registered to a common reference image (by registering and averaging 1200 frames from the center of the session). Regions of interest (ROIs) of active neural cell bodies were detected by computing local correlation (3 by 3 pixel neighborhood, threshold at correlation coefficients > 0.9; customized MATLAB software) and identifying spatially connected pixels, selecting ROIs with near-circular

shapes (maximum length/width aspect ratio < 2). Active axonal boutons were detected with a similar routine with selection parameters adjusted for small ROIs (area size 4-8 pixels). ROIs fluorescence time courses were generated by averaging all pixels in an ROI, followed by subtracting the averaged neuropil signals in the surrounding ring (morphological dilation, ring size matched to the ROI, nonoverlapping with neighboring ROIs) and correcting for slow baseline drift. Raw calcium time courses ($\Delta F/F_0$) were expressed as fractional changes to the baseline fluorescence.

Selection of responsive and reliable cells and axonal boutons.

The selection process was described in our previous study (Han et al., 2022). A cellular or axonal ROI was classified as responsive if the median time courses computed across trials showed a response peak with magnitude > 3x standard deviation of the pre-stimulus activity (averaged > 2 seconds) for over a continuous period > 1 second for at least one stimulus condition. Cells/boutons responding to the visual stimulus offset but not during visual stimulus epochs were excluded from the analysis. ROIs were selected based on a response reliability index, which is defined as the 75th percentile of the cross-trial correlation coefficients of the de-randomized response time courses. ROIs with a reliability index > 0.3 were selected for further analysis. Neurons/boutons' response amplitudes were calculated as the average $\Delta F/F_0$ over the duration of the stimulus epochs.

Spatiotemporal tuning analysis

Responses were described by two-dimensional elliptical Gaussian functions (Andermann et al., 2011; Priebe et al., 2003):

$$R(sf, tf) = Aexp(-\frac{(\log_2 sf - \log_2 sf_0)^2}{2(\sigma_{sf})^2})exp(-\frac{(\log_2 tf - g(sf))^2}{2(\sigma_{tf})^2})$$

where A is the peak response amplitude, sf_0 and tf_0 are the peak spatial and temporal frequencies, σ_{sf} and σ_{tf} are the spatial and temporal frequency tuning widths, and

$$g(sf) = \xi(log_2 sf - log_2 sf_0) + log_2 tf_0$$

In this expression, ξ is the speed tuning index that captures the slant in the spatiotemporal frequency space. Model parameters were estimated by searching for the model fit with least

squared errors in respect to the raw responses (MATLAB *lsqcurvefit* function). Peak speed is defined as the ratio between peak temporal frequency and peak spatial frequency.

Comparison of spatiotemporal peak frequencies distributions

A two-sample two-dimensional Kolmogorov-Smirnov test (2d-KS test) (Peacock, 1983) was used to compare the distributions of neuronal populations in the spatiotemporal frequency space (Figure 1G-H, 4A-D, S4). The yielded distance and significant level (p-value) were reported.

Hierarchical bootstrapping

To measure the average functional properties of visual areas of pathways with the consideration of inter-animal variability, hierarchical datasets were constructed using a hierarchical bootstrapping approach (Han et al., 2022). Each hierarchical dataset was consisting of 1000 random subsamples (with replacement), each of which was consisting of equal numbers of data points from equal numbers of animals (typically, 50 data points per mouse, 5 mice per group). Then the metrics of interest for each subsample were calculated, then the means and distributions of the metrics across subsamples were obtained. All the following analyses used hierarchical bootstrapping.

Average tuning similarity

The overall functional bias of a group of neurons was measured as the bootstrap average spatiotemporal tuning map across neurons. Briefly, the average of neurons' peak-normalized SFTF maps in each subsample was obtained, and the means across subsamples were defined as the bootstrap average SFTF tuning maps (Figure 1E, 3A-C top, 5E, 6E, 7D, S6D). Average tuning similarity between areas or pathways was calculated as pairwise Pearson's correlation coefficients between bootstrap average SFTF tuning maps of the compared neuron groups (Figure 1F, S3C).

Comparison of population tuning similarity

To determine whether the functional similarity between a pair of neuronal populations (i.e., pathways or areas) is different from other pairs, the distributions of functional similarity (obtained using hierarchical bootstrapping) of the two pairs were compared. To do so, we repeatedly selected random subsets of neurons from each cell group, calculated the average SFTF tuning maps, performed pairwise Pearson's correlation, and compared the distributions of correlation coefficients across bootstraps. For example, to determine whether the similarity between

populations A and B is higher than that between populations C and D, hierarchical bootstrap subsamples for each population were generated (subsample A-D) and the averages of neurons' peak-normalized SFTF maps in each subsample were calculated (map A-D). To obtain the distributions of tuning similarity, which is referred to as population tuning similarity, between populations A and B for instance, the Pearson's correlation coefficients between maps A and B (r_{AB}) in each subsampling were calculated and the distributions of r_{AB} across subsamples were obtained. Tuning difference is defined as 1 minus the correlation coefficient (Figure 3A-C, bottom left). Then Cohen's d was used to report the differences between the distributions of r_{AB} and r_{CD} (Figure 3A-C bottom panels, 5E, 6F, 7E-F, S3B, S6E-G). d<0.2 means small difference, 0.2<d<1.8 means medium difference, d>1.8 means large differences.

Comparison of peak frequencies

To determine whether neuronal populations projecting to different areas have different functional biases (Figure 3G), the mean and standard error of the mean of each population were obtained using hierarchical bootstrapping. Briefly, the mean peak spatial and temporal frequencies (μ_{SF}, μ_{TF}) of each random subsample were obtained, and the means and standard deviations of μ_{SF} and μ_{TF} across subsamples (that is the mean and standard error of the mean of the population) were obtained and used to calculate the differences between populations.

References

Andermann, M.L., Kerlin, A.M., Roumis, D.K., Glickfeld, L.L., and Reid, R.C. (2011). Functional specialization of mouse higher visual cortical areas. Neuron *72*, 1025–1039.

Beltramo, R., and Scanziani, M. (2019). A collicular visual cortex: Neocortical space for an ancient midbrain visual structure. Science (80-.). *363*, 64–69.

Bennett, C., Gale, S.D., Garrett, M.E., Newton, M.L., Callaway, E.M., Murphy, G.J., and Olsen, S.R. (2019). Higher-Order Thalamic Circuits Channel Parallel Streams of Visual Information in Mice. Neuron *102*, 477–492.e5.

Blot, A., Roth, M.M., Gasler, I., Javadzadeh, M., Imhof, F., and Hofer, S.B. (2021). Visual intracortical and transthalamic pathways carry distinct information to cortical areas. Neuron *109*, 1996–2008.e6.

La Chioma, A., Bonhoeffer, T., and Hübener, M. (2019). Area-Specific Mapping of Binocular Disparity across Mouse Visual Cortex. Curr. Biol. *29*, 2954–2960.e5.

Cossell, L., Iacaruso, M.F., Muir, D.R., Houlton, R., Sader, E.N., Ko, H., Hofer, S.B., and Mrsic-Flogel, T.D. (2015). Functional organization of excitatory synaptic strength in primary visual cortex. Nature *518*, 399–403.

D'Souza, R.D., Wang, Q., Ji, W., Meier, A.M., Kennedy, H., Knoblauch, K., and Burkhalter, A. (2022). Hierarchical and nonhierarchical features of the mouse visual cortical network. Nat. Commun. *13*, 1–14.

Van Essen, D.C. (2005). Corticocortical and thalamocortical information flow in the primate visual system. Prog. Brain Res. *149*, 173–185.

Felleman, D.J., and Van Essen, D.C. (1991). Distributed hierarchical processing in the primate cerebral cortex. Cereb. Cortex *1*, 1–47.

Gale, S.D., and Murphy, G.J. (2014). Distinct representation and distribution of visual information by specific cell types in mouse superficial superior colliculus. J. Neurosci. *34*, 13458–13471.

Gămănuţ, R., and Shimaoka, D. (2021). Anatomical and functional connectomes underlying hierarchical visual processing in mouse visual system. Brain Struct. Funct.

Gămănuţ, R., Kennedy, H., Toroczkai, Z., Ercsey-Ravasz, M., Van Essen, D.C., Knoblauch, K., and Burkhalter, A. (2018). The Mouse Cortical Connectome, Characterized by an Ultra-Dense Cortical Graph, Maintains Specificity by Distinct Connectivity Profiles. Neuron *97*, 698–715.e10.

Glickfeld, L.L., Andermann, M.L., Bonin, V., and Reid, R.C. (2013). Cortico-cortical projections in mouse visual cortex are functionally target specific. Nat. Neurosci. *16*, 219–226.

Goldey, G.J., and Andermann, M.L. (2014). Simultaneous Two-Photon Calcium Imaging of Entire Cortical Columns. 23–32.

Goodale, M. a, and Milner, A.D. (1992). Separate visual pathways for perception and action. Trends Neurosci. *15*, 20–25.

Han, X., Vermaercke, B., and Bonin, V. (2022). Diversity of spatiotemporal coding reveals specialized visual processing streams in the mouse cortex. Nat. Commun. *13*, 3249.

Han, Y., Kebschull, J.M., Campbell, R.A.A., Cowan, D., Imhof, F., Zador, A.M., and Mrsic-Flogel, T.D. (2018). The logic of single-cell projections from visual cortex. Nature *556*, 51–56.

Harris, J.A., Mihalas, S., Hirokawa, K.E., Whitesell, J.D., Choi, H., Bernard, A., Bohn, P., Caldejon, S., Casal, L., Cho, A., et al. (2019). Hierarchical organization of cortical and thalamic connectivity. Nature *575*, 195–202.

Hebart, M.N., and Hesselmann, G. (2012). What visual information is processed in the human dorsal stream? J. Neurosci. *32*, 8107–8109.

Hu, F., Kamigaki, T., Zhang, Z., Zhang, S., Dan, U., and Dan, Y. (2019). Prefrontal Corticotectal Neurons Enhance Visual Processing through the Superior Colliculus and Pulvinar Thalamus. Neuron *104*, 1141–1152.e4.

Huh, C.Y., Peach, J.P., Bennett, C., Vega, R.M., and Hestrin, S. (2018). Feature-Specific Organization of Feedback Pathways in Mouse Visual Cortex. Curr. Biol. 1–7.

Juavinett, A.L., Kim, E.J., Collins, H.C., and Callaway, E.M. (2020). A systematic topographical relationship between mouse lateral posterior thalamic neurons and their visual cortical projection targets. J. Comp. Neurol. *528*, 95–107.

Kim, E.J., Juavinett, A.L., Kyubwa, E.M., Jacobs, M.W., and Callaway, E.M. (2015). Three Types of Cortical Layer 5 Neurons That Differ in Brain-wide Connectivity and Function. Neuron *88*, 1253–1267.

Kim, E.J., Zhang, Z., Huang, L., Ito-Cole, T., Jacobs, M.W., Juavinett, A.L., Senturk, G., Hu, M., Ku, M., Ecker, J.R., et al. (2020). Extraction of Distinct Neuronal Cell Types from within a Genetically Continuous Population. Neuron *107*, 274–282.e6.

Kim, M.H., Znamenskiy, P., Iacaruso, M.F., and Mrsic-Flogel, T.D. (2018). Segregated Subnetworks of Intracortical Projection Neurons in Primary Visual Cortex. Neuron *100*, 1313–1321.e6.

Ko, H., Hofer, S.B., Pichler, B., Buchanan, K.A., Sjöström, P.J., and Mrsic-Flogel, T.D. (2011). Functional specificity of local synaptic connections in neocortical networks. Nature *473*, 87–91.

Lee, W.-C.A.C.A., Bonin, V., Reed, M., Graham, B.J., Hood, G., Glattfelder, K., and Reid, R.C. (2016). Anatomy and function of an excitatory network in the visual cortex. Nature *532*, 370–374.

Li, L.Y., Li, Y.T., Zhou, M., Tao, H.W., and Zhang, L.I. (2013a). Intracortical multiplication of thalamocortical signals in mouse auditory cortex. Nat. Neurosci. *16*, 1179–1181.

Li, Y.T., Ibrahim, L.A., Liu, B.H., Zhang, L.I., and Tao, H.W. (2013b). Linear transformation of thalamocortical input by intracortical excitation. Nat. Neurosci. *16*, 1324–1330.

Lien, A.D., and Scanziani, M. (2013). Tuned thalamic excitation is amplified by visual cortical circuits. Nat. Neurosci. *16*, 1315–1323.

Lur, G., Vinck, M.A., Tang, L., Cardin, J.A., and Higley, M.J. (2016). Projection-Specific Visual Feature Encoding by Layer 5 Cortical Subnetworks. Cell Rep. *14*, 2538–2545.

Marshel, J.H., Garrett, M.E., Nauhaus, I., and Callaway, E.M. (2011). Functional specialization of seven mouse visual cortical areas. Neuron *72*, 1040–1054.

Miller-Hansen, A.J., and Sherman, S.M. (2022). Conserved patterns of functional organization between cortex and thalamus in mice. Proc. Natl. Acad. Sci. *119*, 1–12.
Mishkin, M., Ungerleider, L.G., and Macko, K.A. (1983). Object vision and spatial vision: two cortical pathways. Trends Neurosci. *6*, 414–417.
Munz, M., Bharioke, A., Kosche, G., Moreno-Juan, V., Brignall, A., Rodrigues, T.M., Graff-Meyer, A., Ulmer, T., Haeuselmann, S., Pavlinic, D., et al. (2023). Pyramidal neurons form active, transient, multilayered circuits perturbed by autism-associated mutations at the inception of neocortex. Cell 1–20.
Murakami, T., Matsui, T., and Ohki, K. (2017). Functional segregation and development of mouse higher visual areas. J. Neurosci. *37*, 9424–9437.
Murgas, K.A., Wilson, A.M., Michael, V., and Glickfeld, L.L. (2020). Unique Spatial Integration in Mouse Primary Visual Cortex and Higher Visual Areas. J. Neurosci. *40*, 1862–1873.
Nassi, J.J., and Callaway, E.M. (2009). Parallel processing strategies of the primate visual system. Nat. Rev. Neurosci. *10*, 360–372.
Niell, C.M., and Stryker, M.P. (2008). Highly selectaive receptive fields in mouse visual cortex. J. Neurosci. *28*, 7520–7536.
Orban, G.A. (2008). Higher order visual processing in macaque extrastriate cortex. Physiol. Rev. *88*, 59–89.
Peacock, J.A. (1983). Two-dimensional goodness-of-fit testing in astronomy. Mon. Not. R. Astron. Soc. *202*, 615–627.
Priebe, N.J., Cassanello, C.R., and Lisberger, S.G. (2003). The neural representation of speed in macaque area MT/V5. J. Neurosci. *23*, 5650–5661.
Sit, K.K., and Goard, M.J. (2020). Distributed and retinotopically asymmetric processing of coherent motion in mouse visual cortex. Nat. Commun. *11*, 1–14.
Tanaka, K. (1996). Inferotemporal cortex and object vision. Annu. Rev. Neurosci. *19*, 109–139.
Tasic, B., Yao, Z., Graybuck, L.T., Smith, K.A., Nguyen, T.N., Bertagnolli, D., Goldy, J., Garren, E., Economo, M.N., Viswanathan, S., et al. (2018). Shared and distinct transcriptomic cell types across neocortical areas. Nature *563*, 72–78.
Tervo, D.G.R., Hwang, B.Y., Viswanathan, S., Gaj, T., Lavzin, M., Ritola, K.D., Lindo, S., Michael, S., Kuleshova, E., Ojala, D., et al. (2016). A Designer AAV Variant Permits Efficient Retrograde Access to Projection Neurons. Neuron *92*, 372–382.
Tohmi, M., Meguro, R., Tsukano, H., Hishida, R., and Shibuki, K. (2014). The Extrageniculate Visual Pathway Generates Distinct Response Properties in the Higher Visual Areas of Mice. Curr. Biol. 1–11.
de Vries, S.E.J.J., Lecoq, J.A., Buice, M.A., Groblewski, P.A., Ocker, G.K., Oliver, M., Feng, D., Cain, N., Ledochowitsch, P., Millman, D., et al. (2020). A large-scale standardized physiological survey reveals functional organization of the mouse visual cortex. Nat. Neurosci. *23*, 138–151.
Wang, Q., and Burkhalter, A. (2007). Area Map of Mouse Visual Cortex. Jounal Comp. Neurol. *505*, 337–

351.
Wang, Q., Sporns, O., and Burkhalter, A. (2012). Network analysis of corticocortical connections reveals ventral and dorsal processing streams in mouse visual cortex. J. Neurosci. *32*, 4386–4399.
Wekselblatt, J.B., Flister, E.D., Piscopo, D.M., and Niell, C.M. (2016). Large-scale imaging of cortical dynamics during sensory perception and behavior. J. Neurophysiol. jn.01056.2015.
Yao, S., Wang, Q., Hirokawa, K.E., Ouellette, B., Ahmed, R., Bomben, J., Brouner, K., Casal, L., Caldejon, S., Cho, A., et al. (2022). A whole-brain monosynaptic input connectome to neuron classes in mouse visual cortex. Nat. Neurosci. 2022 262 *26*, 350–364.
Zhang, Y., Rózsa, M., Liang, Y., Bushey, D., Wei, Z., Zheng, J., Reep, D., Broussard, G.J., Tsang, A., Tsegaye, G., et al. (2023). Fast and sensitive GCaMP calcium indicators for imaging neural populations. Nature *615*, 884–891.
Zhuang, J., Ng, L., Williams, D., Valley, M., Li, Y., Garrett, M., and Waters, J. (2017). An extended retinotopic map of mouse cortex. Elife *6*, 1–27.

Acknowledgements

We are grateful to Ben Vermaercke for supporting the imaging setup and image processing, Asli Ayaz, and Karl Farrow for feedback, discussions, and comments on earlier versions of the manuscript. This work was supported by Neuro-Electronics Research Flanders (V.B.), FWO grants G0D0516N (V.B.), G0C1220N (V.B.), and KU Leuven Research Council grant C14/16/048 (V.B.).

Author contributions

Conceptualization: X.H. and V.B.; Methodology: X.H. and V.B.; Software: X.H.; Investigation: X.H.; Data curation: X.H.; Formal Analysis: X.H. and V.B.; Visualization: X.H. and V.B.; Writing—original draft: X.H.; Writing—review & editing: X.H. and V.B.; Funding acquisition: V.B.; Resources: X.H. and V.B.; Supervision: V.B.

Competing interests

The authors declare no competing interests.

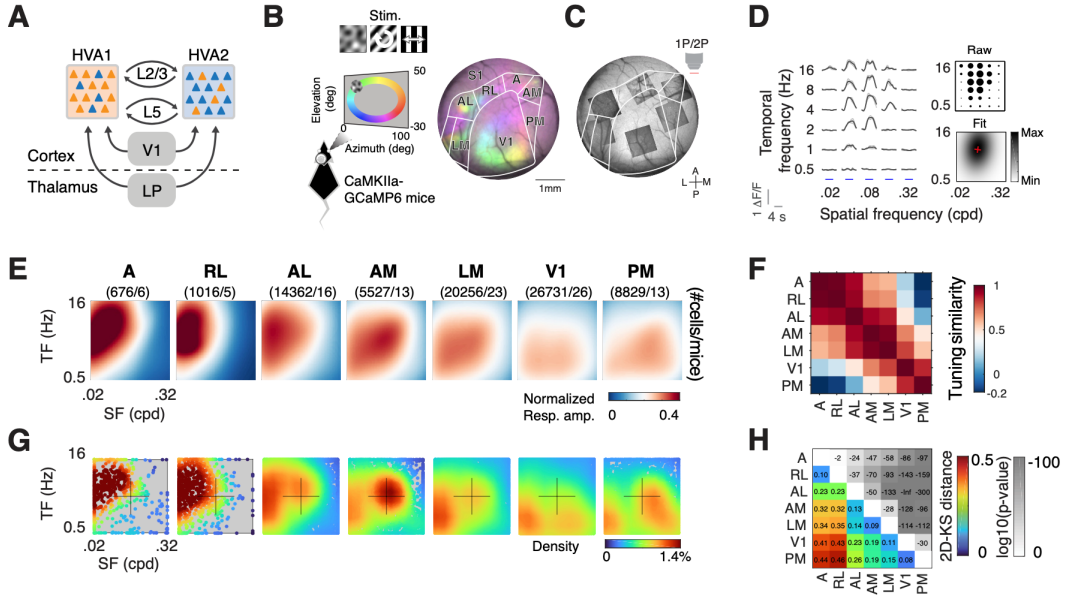

Figure 1. Heterogeneous spatiotemporal tuning underlies specialized HVA representations.

(A) Schematic showing the intracortical and thalamocortical communication pathways between V1, lateral posterior thalamic nucleus (LP), and higher visual areas (HVAs).

(B) Schematic showing the visual stimulation paradigm and an example retinotopic map over the surface of the left visual cortex of a GCaMP6- transgenic mouse (CaMKII-tTA x TRE-GcaMP6s), with areal delineation (white contours). The cortex imaged through a chronic cranial window is color-coded by the location of the visual field evoking the highest neural responses.

(C) Example two-photon fields-of-view over different visual cortical areas, superimposed on a one-photon image of the cortical surface.

(D) Spatiotemporal frequency tuning of an example cortical neuron. Traces are trial-averaged calcium fluorescence changes in response to visual stimuli with distinct combinations of spatial and temporal frequencies. The largest mean response amplitudes (Raw, top right) evoked by the visual stimulus sets were fitted to a 2D Gaussian model (bottom right). Red cross: The neuron's preferred (peak) spatiotemporal frequency.

(E) Distinct averaged spatiotemporal tuning surfaces of neurons across areas. The tuning surfaces were the averages of different subsampling of datasets across animals with hierarchical bootstrapping. The numbers of cells and mice are shown at the top.

(F) Tuning similarity across visual cortical areas. Tuning similarity is calculated as Pearson's correlation coefficients between average tuning maps.

(G) Distinct distributions of peak spatial (SF) and temporal frequencies (TF) of neurons in different areas.

(H) Pair-wise distances of the 2D distributions of peak spatiotemporal frequencies. Two-dimensional Kolmogorov–Smirnov (2D-KS) distances are shown in the lower left triangle. P-values are shown in the upper right triangle.

See also Figure S1.

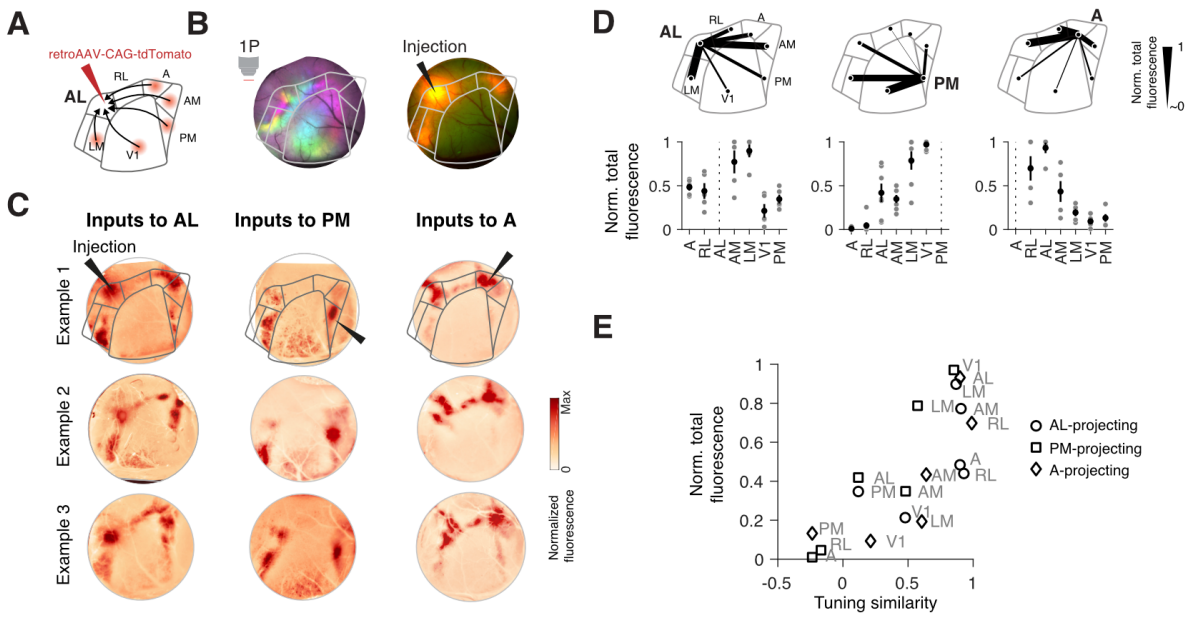

Figure 2. Intracortical inputs to HVAs originate primarily from similarly-tuned visual areas.

(A) Schematic of retrograde tracing of intracortical input pathway.

(B) Widefield images of the cortical surface showing the retinotopic map (left) and tdTomato expression 10 days after the injection of the retrograde virus at area AL (right).

(C) Example cortical input maps resulting from injections of retrograde viruses in different areas (columns) in different mice (rows). Gray contours: area delineation.

(D) Summary of the anatomical intensity of cortical input pathways to areas AL, PM, and A. N=5,8,5 mice, respectively (gray markers). Black markers: mean ± SEM

(E) Scatter plot showing the correlation between the strength of retrograde intracortical labeling and the similarity of visual tuning amongst connected HVAs. The source areas are shown in text and the target areas are represented as different types of markers.

See also Figure S2.

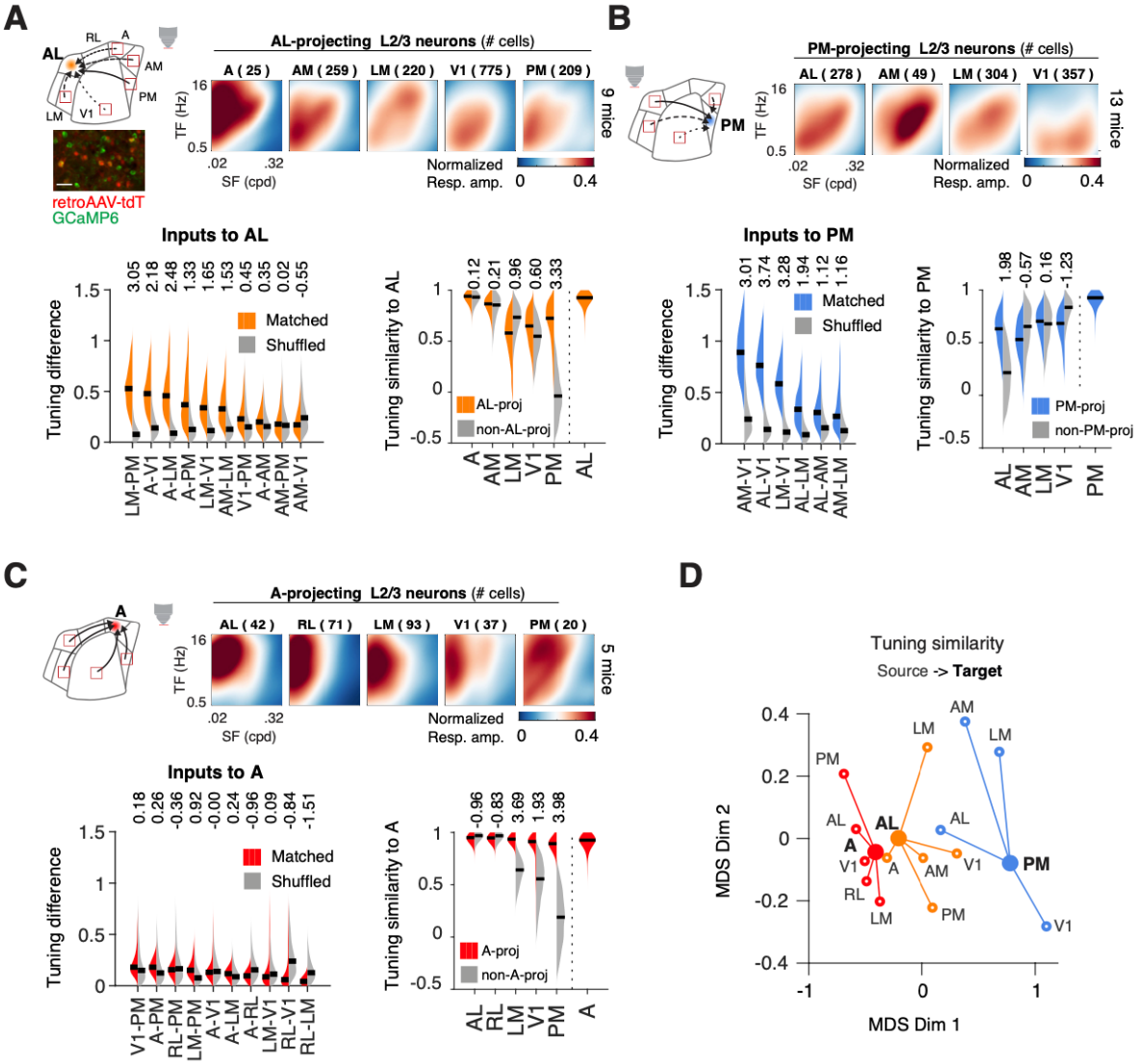

Figure 3. Distinct functional biases of visual inputs from intracortical L2/3 neurons to HVAs.

(A) Diversity and specificity of tuning amongst L2/3 neurons targeting AL. Top left: scheme showing 2-photon imaging of input pathways. Inset at the bottom shows a 2-photon FOV with tdTomato+ retrograde projection neurons and GCaMP6s+ neurons. Top right: summary of average spatiotemporal tuning of retrogradely labeled AL-projecting L2/3 neurons in different areas. Bottom left: Tuning differences between AL-projecting pathways. The differences (colored) were compared to those of the shuffled datasets (gray), and the statistical differences (Cohen's d) were reported as text at the top. Black horizontal bars: median values of each violin distribution. Bottom right: Tuning similarity of AL with the respective input pathways (AL-proj) and the control group (non-AL-proj). The statistical differences (Cohen's d) between the two distributions (AL-proj vs non-AL-proj) are reported as text at the top. As a reference of the within-area variability in AL, the tuning similarity between different subsamples of AL neurons was shown in the rightmost column. Black bars: median values.

(B) Same as (A), for input pathways to area PM.
(C) Same as (A), for input pathways to area A.
(D) 2D-MDS representation of the spatiotemporal tuning similarity between HVAs and L2/3 cortical input pathways. Target HVAs are connected to their respective source areas. MDS: multi-dimensional scaling.

See also Figure S3.

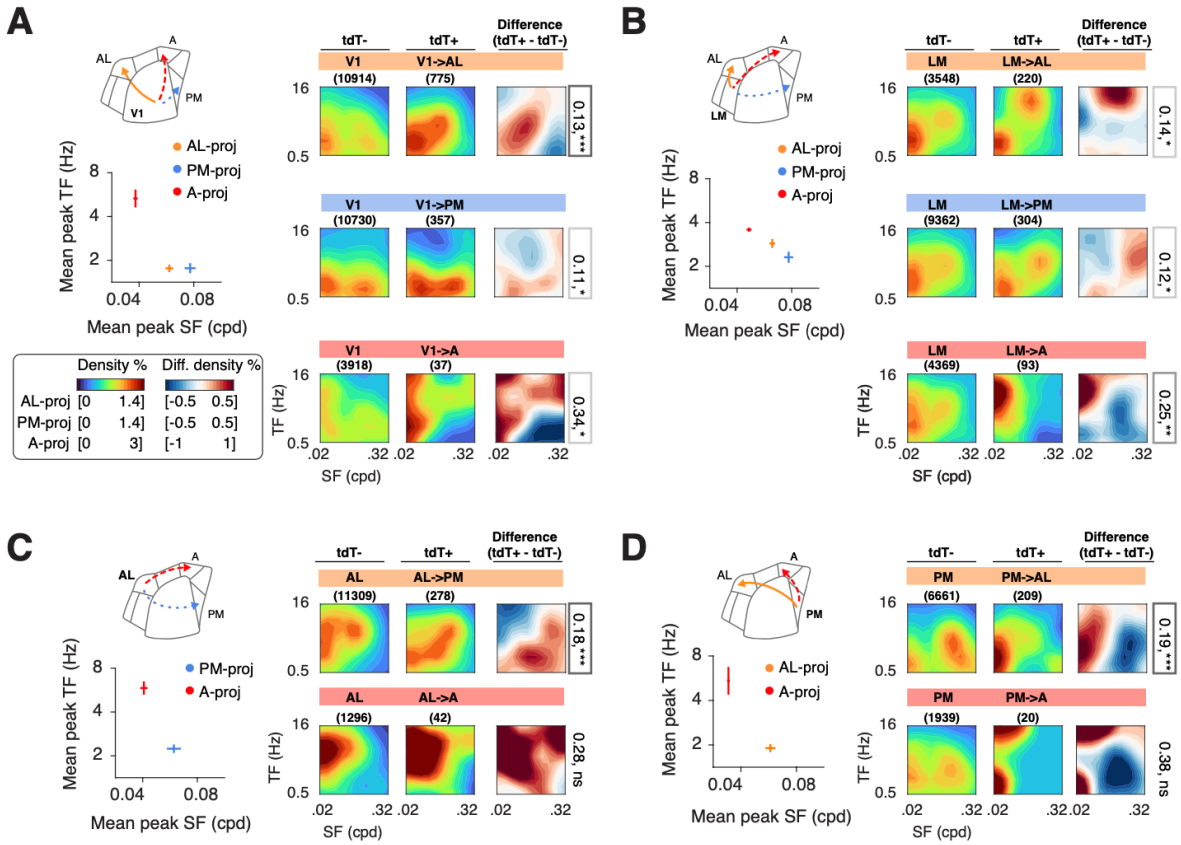

Figure 4. Both lower and higher-order V1 and HVA neurons make target-specific connections to HVAs.

(A) Comparison of the spatiotemporal tuning of V1 neurons projecting to either area AL, PM, or A. Left: Distinct mean peak SF and TF of V1 subpopulations projecting to area AL, PM and A. Means and STD were estimated from the means of bootstrap subsamples of neurons within each group. Right: Density plots showing the distribution of peak spatiotemporal frequencies of V1 L2/3 neurons without (tdT-) and with retrograde labeling (tdT+), and the differences between the two populations. Each row shows the datasets obtained from mice with injections in AL, PM, and A, respectively. 2D-KS distances of the distributions of peak spatiotemporal frequencies between tdT- and tdT+ were shown on the right. The significance levels were shown as * and the boxes. p<0.001: ***; p<0.01:**;p<0.05:*; n.s: no significance. Left bottom: color space represents different ranges for different datasets to avoid saturation. Same color spaces for panels A-D.

(B) Same as (A), for projection neurons in area LM projecting to either area AL, PM or A.

(C) Same as (A), for projection neurons in area AL projecting to either area A or PM.

(D) Same as (A), for projection neurons in area PM projecting to either area A or AL.

See also Figure S4.

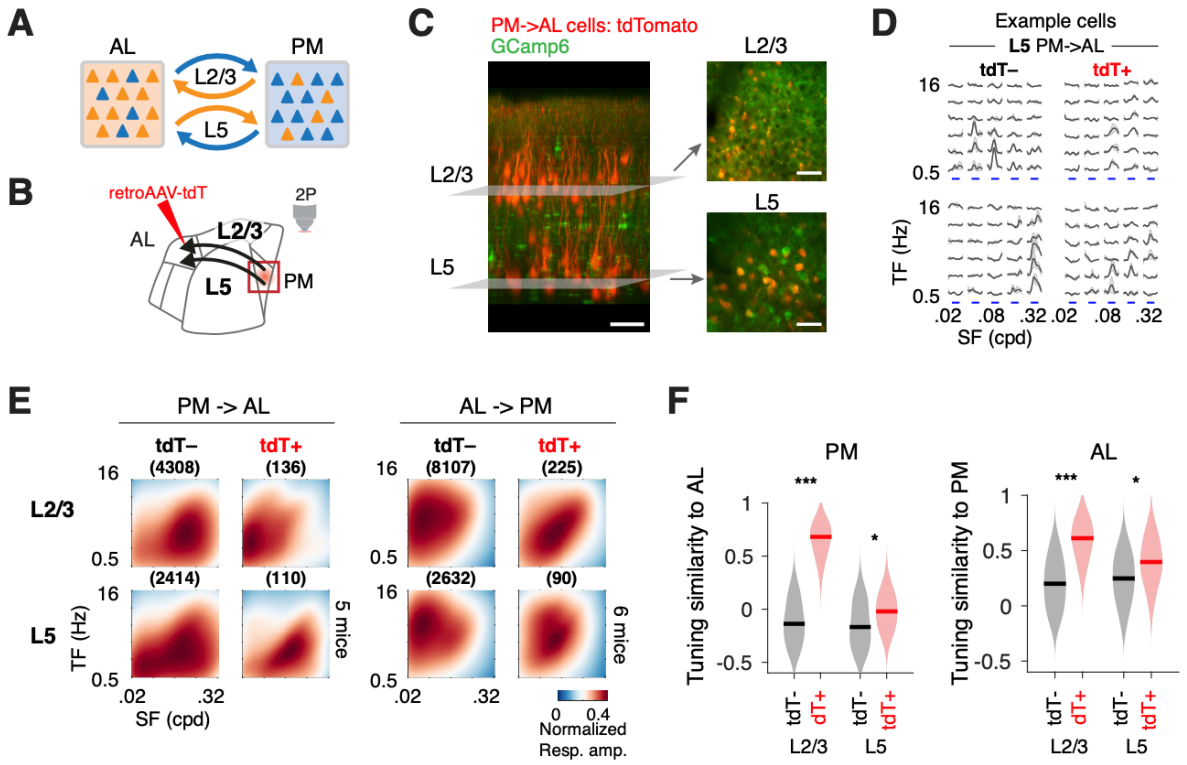

Figure 5. Higher-order L2/3 and L5 projections to HVAs differ in their spatiotemporal tuning and degree of functional target specificity.

(A) Scheme showing L2/3 and L5 intracortical neurons mediate communication pathways between AL and PM.

(B) Experimental scheme showing retrograde labeling and simultaneous 2-photon imaging of both L2/3 and L5 projection neurons.

(C) 2-photon volumetric imaging of GCaMP6-expressing neurons in L2/3 and L5 of area PM with retrograde labeling of PM->AL projecting cells. Left image: side-view of the cortex obtained using in vivo volume imaging. Right image: top-view FOVs at L2/3 and L5.

(D) Example responses of PM L5 neurons with (tdT+) and without retrograde labeling (tdT-) to spatiotemporal visual stimuli.

(E) Average spatiotemporal tuning of tdT- neurons in L2/3 and L5 of PM and AL, and tdT+ neurons mediating reciprocal communication between PM and AL. The numbers of neurons are shown in parentheses.

(F) Bootstrap distribution of tuning similarity of the subpopulation of neurons (PM or AL) of distinct projection targets (tdT+ vs tdT-) and laminar positions (L2/3 vs L5) in relation to the tuning in AL or PM. Blank bars: median values. Cohen's d, d>1.8: ***; d<0.2: *.

See also Figure S5.

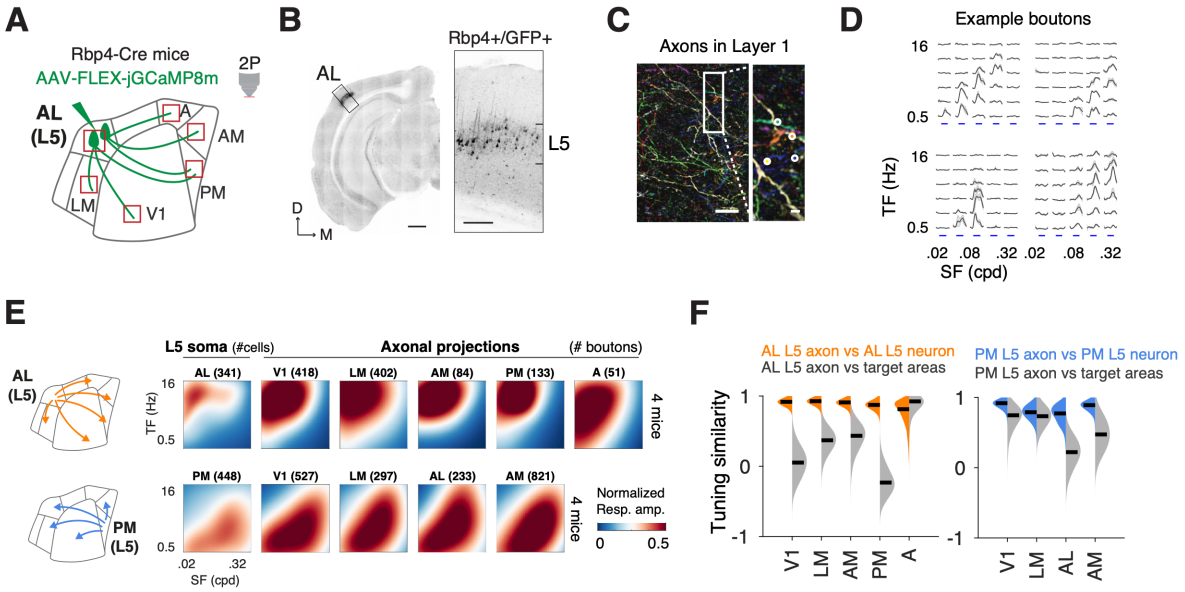

Figure 6. L5 HVA neurons broadcast tuned information across visual cortical areas in a target-independent manner.

(A) Schematic showing the labeling and imaging of axonal projections of L5 neurons. Cre-dependent AAV was delivered to selected HVAs of Rbp4-Cre mice to induce GCaMP8 expression in L5 neurons. Labeled L5 and axonal projections were imaged at across cortical areas using 2P imaging (red boxes).

(B) Coronal slice showing the laminar location and spread of labeled neurons. Scale bar: 1mm. Right: zoom-in at the injection site (black box). Scale bar: 250um.

(C) Example FOV showing axonal projections imaged in cortical layer 1. Axons are color-coded by different spatiotemporal tuning preferences and belong to distinct neurons. Scale bar: 20um. A zoom-in of the white box is shown on the right. White circles show example axonal boutons. Scale bar: 2um.

(D) Example responses to spatiotemporal visual stimuli of the axonal boutons shown in (C).

(E) Average spatiotemporal tuning maps of L5 neurons in AL or PM and their axonal projections in different cortical areas.

(F) Bootstrap distribution of tuning similarity of the L5 axons to the L5 source neurons (colorred) and to the target areas (gray). Black bars: median values.

See also Figure S6.

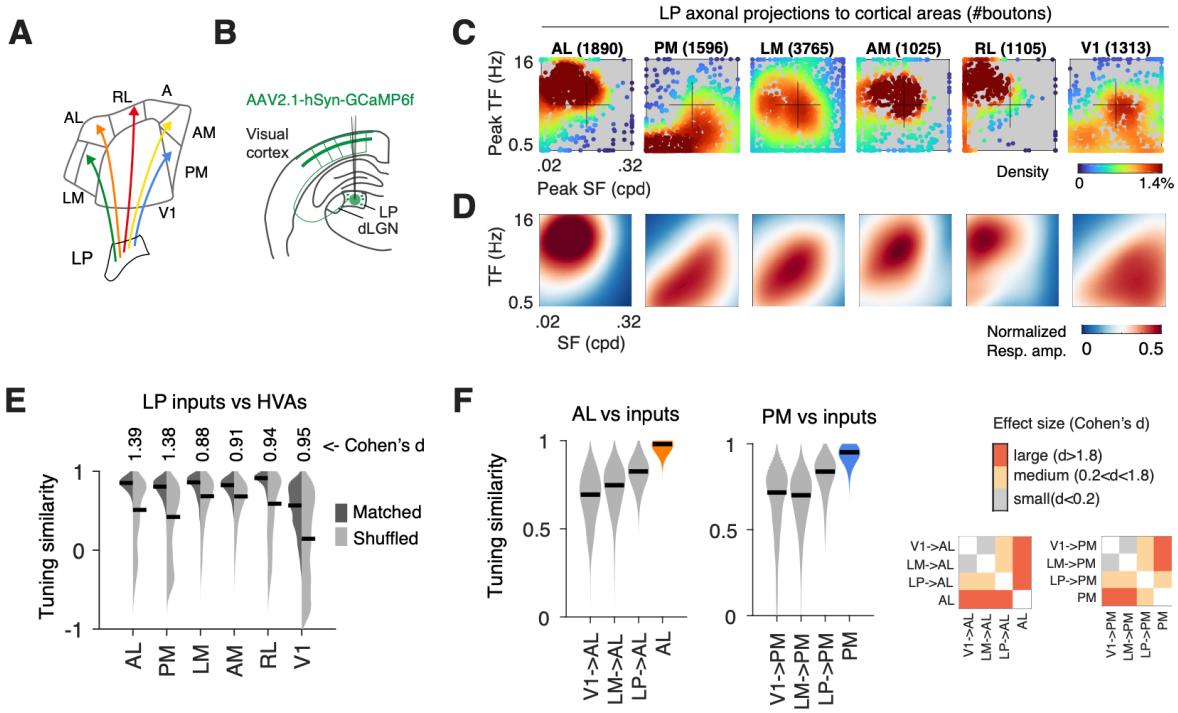

Figure 7. Higher-order thalamocortical LP pathways show high diversity and stronger target-specificity than intracortical pathways.

(A) Schematic of parallel thalamocortical pathways from the lateral posterior thalamus (LP) to different HVAs.

(B) Schematic of labeling and imaging of thalamocortical pathways. LP neurons were labeled with GCaMP6 via the injection of AAV in LP. The axonal projections of LP neurons extending to the cortex were imaged in the superficial layer of different cortical areas using 2P calcium imaging.

(C) Distributions of peak SF and TF of axonal boutons of LP neurons in different cortical areas.

(D) Average spatiotemporal tuning maps of axonal boutons of LP neurons in different cortical areas.

(E) Bootstrap distribution of tuning similarity of LP input pathways to matched cortical targets versus the similarity to shuffled targets. Pair-wise statistical differences between matched and shuffled groups (Cohen'd) are shown on the top. Black bars: median values.

(F) Bootstrap distribution of the tuning similarity of different input pathways (from LP, V1, or, LM respectively) to area AL (left) or PM (right). Black bars: median values. Right panes: Matrices showing the pair-wise statistical differences between cell groups measured as effect sizes (Cohen's d).

See also Figure S7.

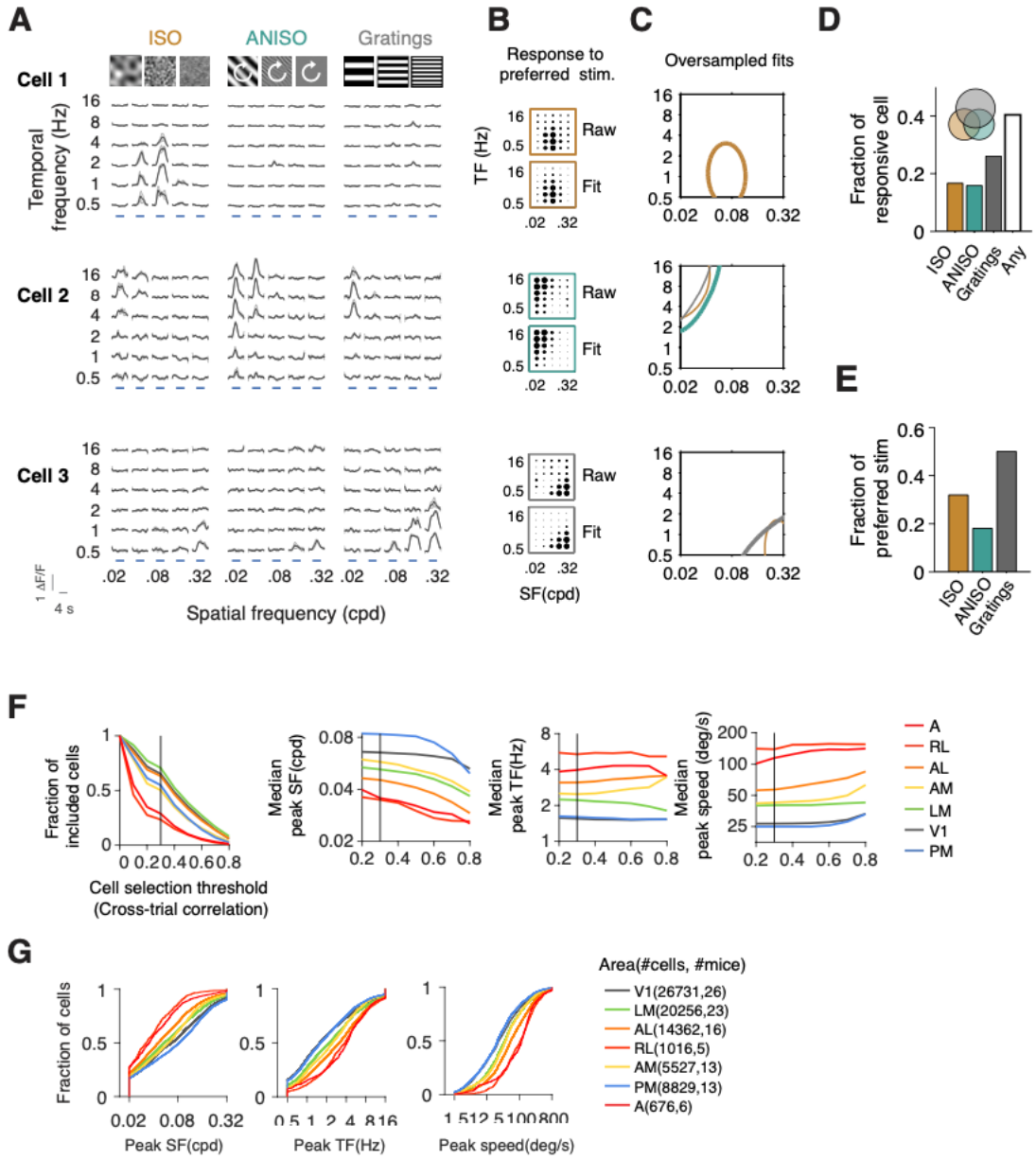

Figure S1. Characterization of spatiotemporal tuning of HVA neurons using noise and gratings stimuli, related to Figure 1.

(A) Visual responses (traces of calcium fluorescent intensity) of three example cells (rows) to three spatiotemporal visual stimuli (from left to right: isotropic noise, anisotropic noise, drifting gratings). The same color code for the three stimuli are used throughout panels A-E.

(B) Dot plots showing mean response amplitudes (raw) and the model fits of the strongest responses to the three stimuli.

(C) Contour plots showing the fits (at 50% peak amplitudes) of responses to noise and gratings visual stimuli. The fits with the strongest response amplitudes are shown with thicker contours.

(D) Bar plot showing the fraction of neurons with reliable visual responses to each stimulus set and to any of them.
(E) Bar plot showing the fraction of neurons that prefer isotropic noise, anisotropic noise and drifting gratings respectively.
(F) Impact of the cell selection threshold (minimal cross-trial variability) on the fraction of included neurons, median peak spatial frequency, median peak temporal frequency, and median peak speed (from left to right). The threshold was set to 0.3 in the current study.
(G) Cumulative distributions of peak spatial frequency, peak temporal frequency and peak speed of L2/3 neurons in different visual areas.

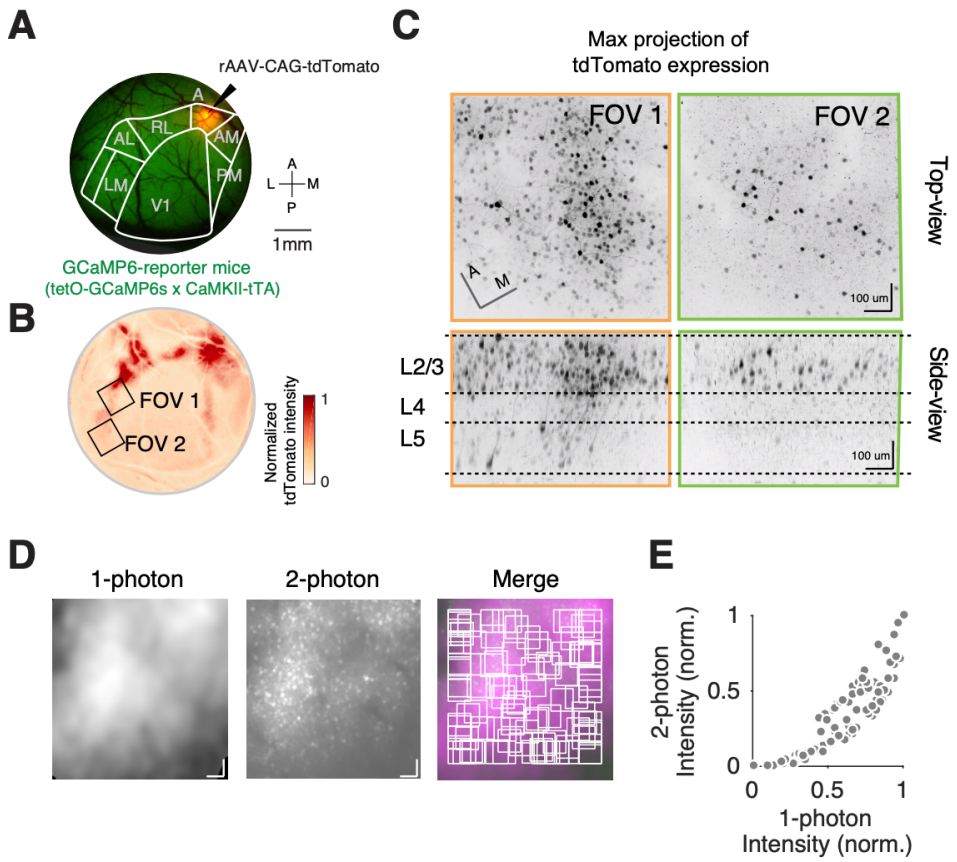

Figure S2. Mesoscopic fluorescent intensity of retrograde labeling broadly correlates with the density of retrogradely labeled neurons, related to Figure 2.

(A) Example widefield fluorescent image of a cranial window of a GCaMP6-mice with the injection of retrograde AAV in area A. White contour: area delineation.

(B) Cortical input maps as a filtered image of the raw image shown in (A). Two FOVs (black boxes) with distinct intensity levels were further inspected with 2P volumetric imaging (results shown in panel C).

(C) Max projections of the tdTomato expression showing the top-view and side-view of FOV1 and 2.

(D) Comparing signals of 1P FOV and corresponding 2P FOV. A 2D Gaussian filter was applied to the 2P FOV to approximate the effect of light scattering on 1P imaging. The average intensities of different regions of the FOV are plotted in (E).

(E) Scatter plot showing the correspondence of the intensity of retrograde labeling measured using 1P or 2P imaging.

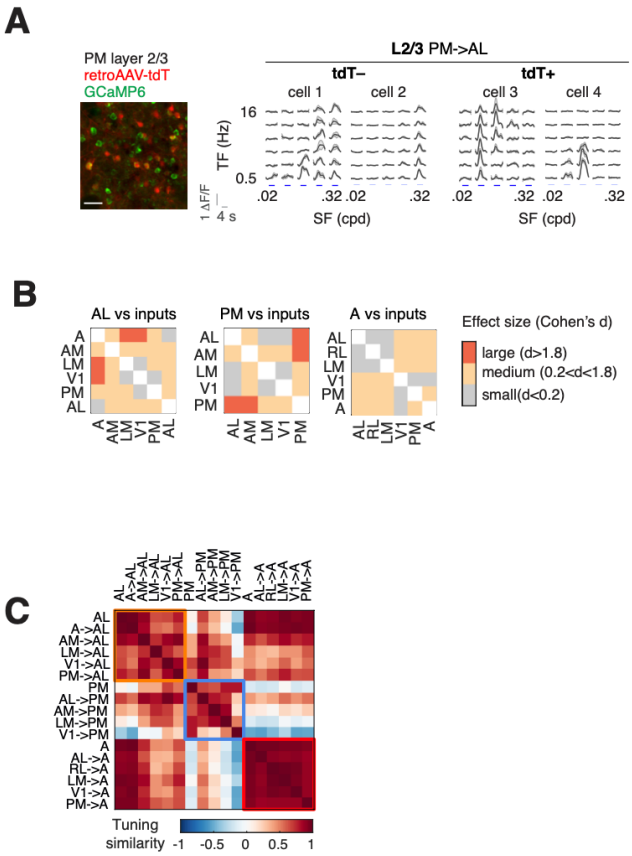

Figure S3. L2/3 intracortical pathways are functionally target specific, related to Figure 3.

(A) Left: example FOV showing GCaMP6-expressing L2/3 neurons (green) in area PM with a retrogradely labeled subpopulation that projects to area AL (red and yellow). Scale bar: 100um. Right: example responses to spatiotemporal visual stimuli.

(B) Matrices showing Cohen's d between the target specificity of input pathways to areas AL, PM, and A, respectively. The distributions were shown in the bottom right panels in Figure 3A-C.

(C) Correlation matrix showing the tuning similarity (Pearson's correlation coefficients between SFTF tuning maps) across HVAs (AL, PM and A) and their L2/3 intracortical input pathways. HVAs and their respective input pathways are grouped and shown in the boxes.

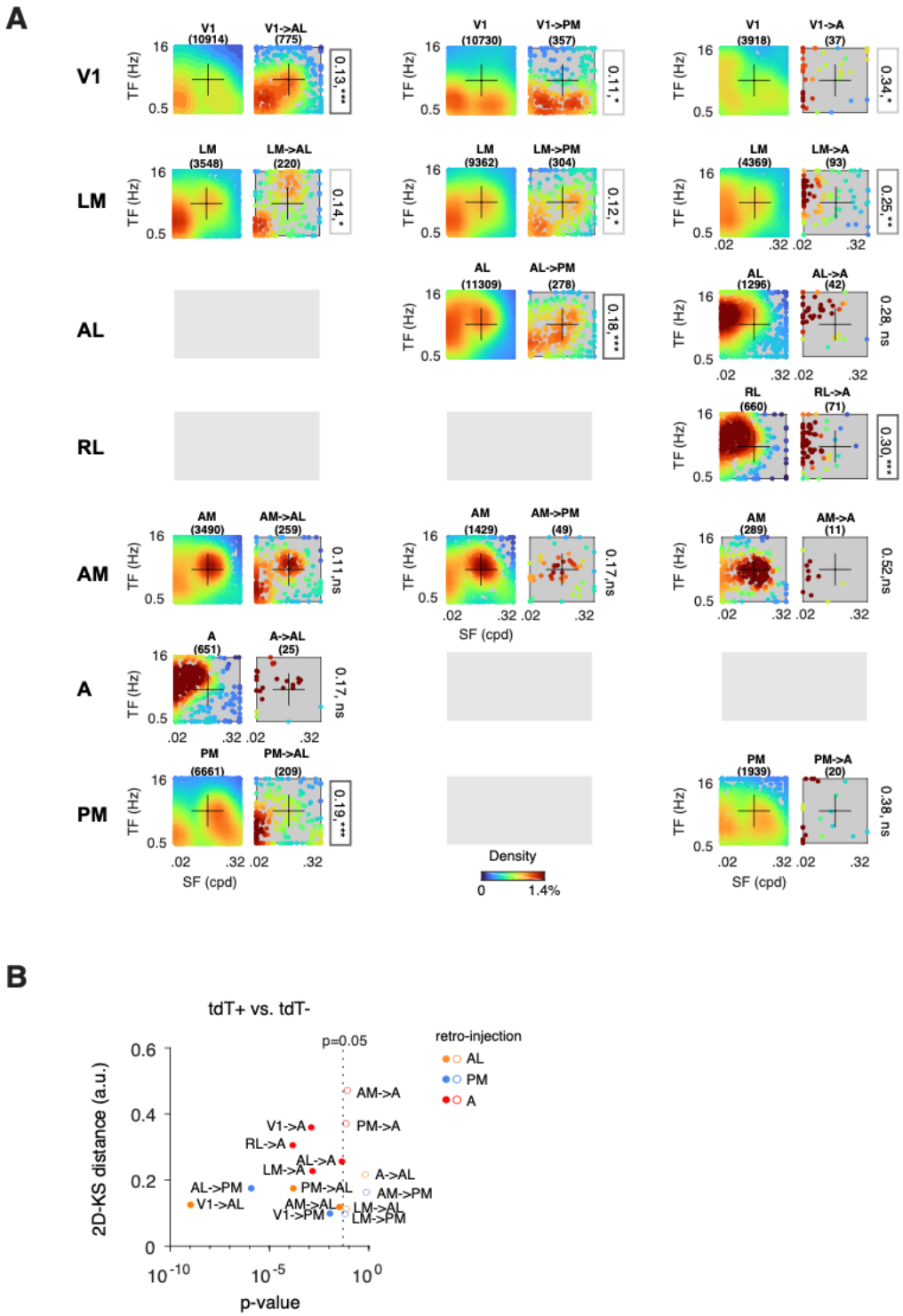

Figure S4. Statistical comparisons of the peak spatiotemporal frequencies between subpopulations of L2/3 intracortical neurons, related to Figure 4.

(A) Density scatter plots showing the distribution of peak spatiotemporal frequencies of retrogradely labeled L2/3 projection neurons and non-labeled L2/3 neurons in different areas (by rows) with retrograde virus injections in AL, PM, or A (by columns). Datapoints

are color-coded by estimated local density. The density maps are replotted as the contour plots in Figure 3. 2D-KS distances of the distributions of peak spatiotemporal frequencies between tdT- and tdT+ were shown on the right. The significance levels were shown as * and the boxes. $p<0.001$: ***; $p<0.01$:**;$p<0.05$:*;n.s: no significance.

(B) Scatter plot showing the p-value and 2D-KS distances between the tdT- and tdT+ neurons in each dataset. Datasets with significant differences ($p<0.05$, dash line) are shown as solid dots, otherwise circles.

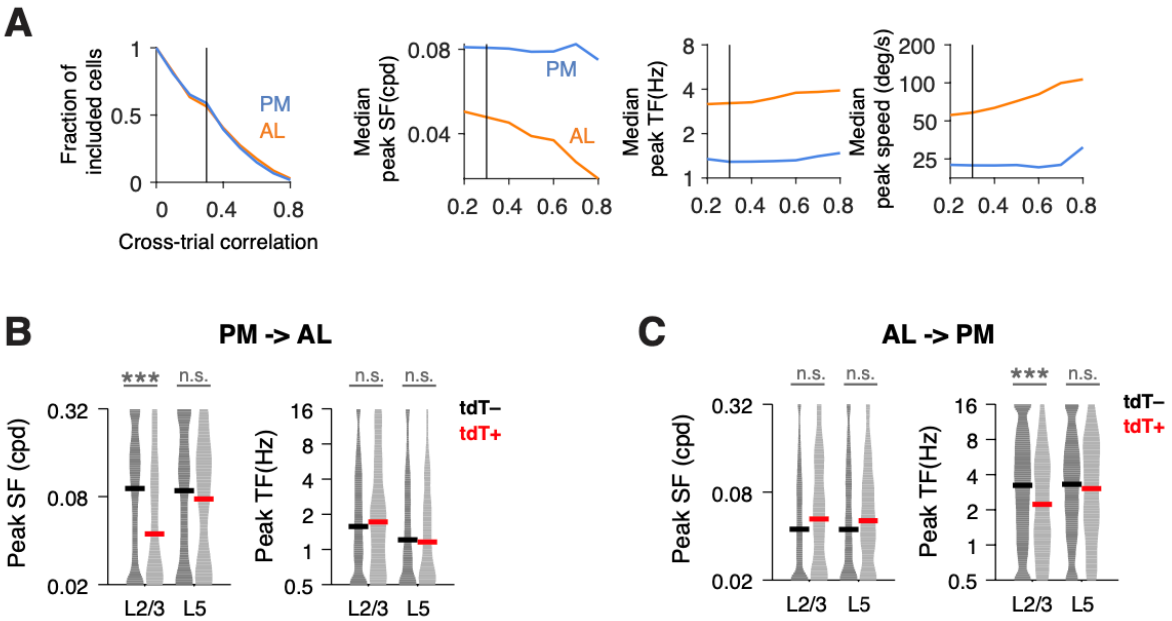

Figure S5. Functional characterization of L5 neurons, related to Figure 5.

(A) Effect of the cell selection threshold (minimal cross-trial variability) on the fraction of included neurons, peak spatial frequency, peak temporal frequency, and peak speed.

(B) Distribution of peak SF and peak TF of tdT- and AL-projecting tdT+ neurons in L2/3 and L5 of area PM. Horizontal bars: median values.

(C) Same as (B), for tdT- and PM-projecting tdT+ neurons in area AL.

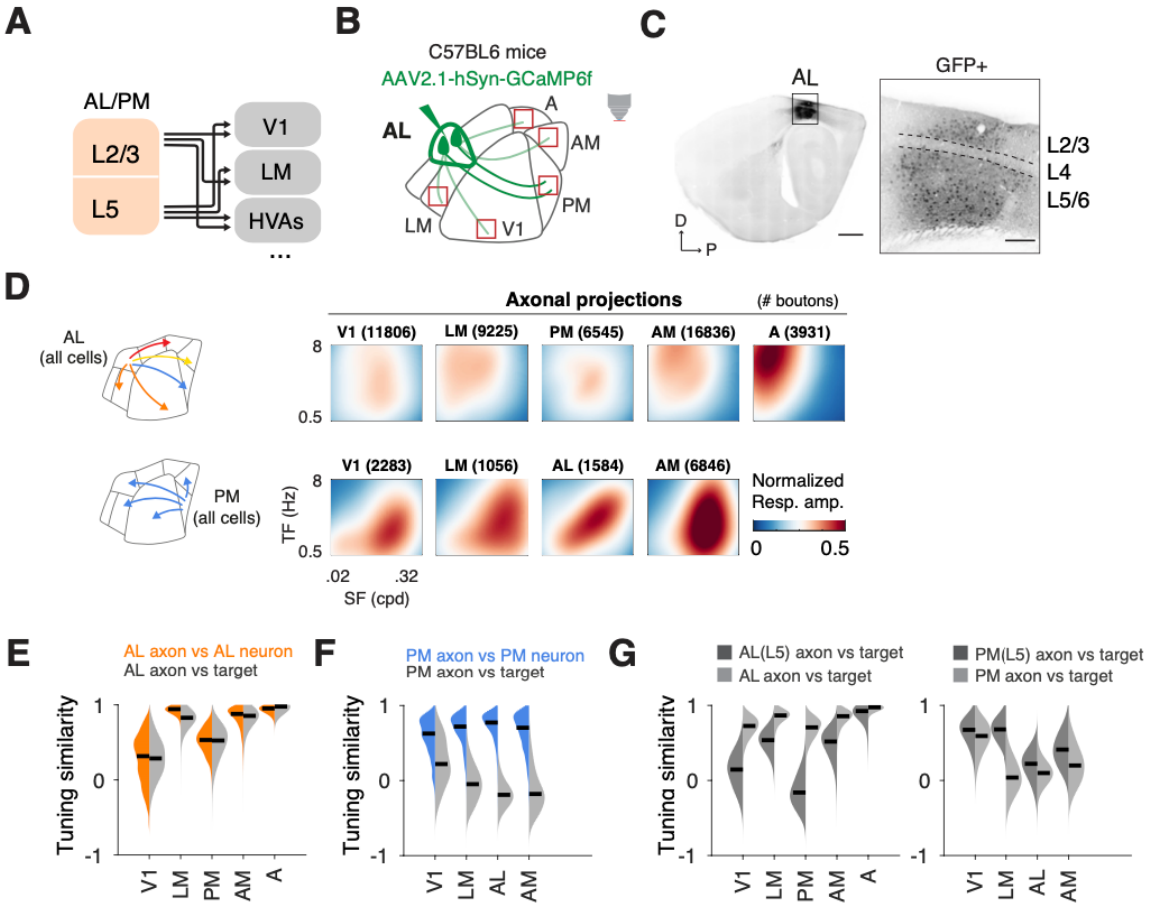

Figure S6. AL, not PM, sends overall target-specific information to distinct cortical areas, related to Figure 6.

(A) Schematic showing the convergency of L2/3 and L5 pathways in other cortical areas.

(B) Schematic showing the approach to label axons from all projection neurons in area AL by targeted viral injections. Labeled L5 and axonal projections were imaged at across cortical areas using 2P imaging (red boxes).

(C) Sagittal slice showing the laminar location and spread of labeled neurons. Scale bar: 1mm. Right: zoom-in at the injection site (black box). Scale bar: 200um.

(D) Average spatiotemporal tuning maps of the axonal projections from AL or PM in different cortical areas.

(E) Bootstrap distribution of tuning similarity of the AL axons to AL neurons (orange) and to neurons in the target areas (gray).

(F) Same as (E), for PM axons.

(G) Bootstrap distribution of tuning similarity of the AL (or PM) axons, either from L5 neurons (dark gray) or from multi-layer neurons (light gray), to individual target areas.

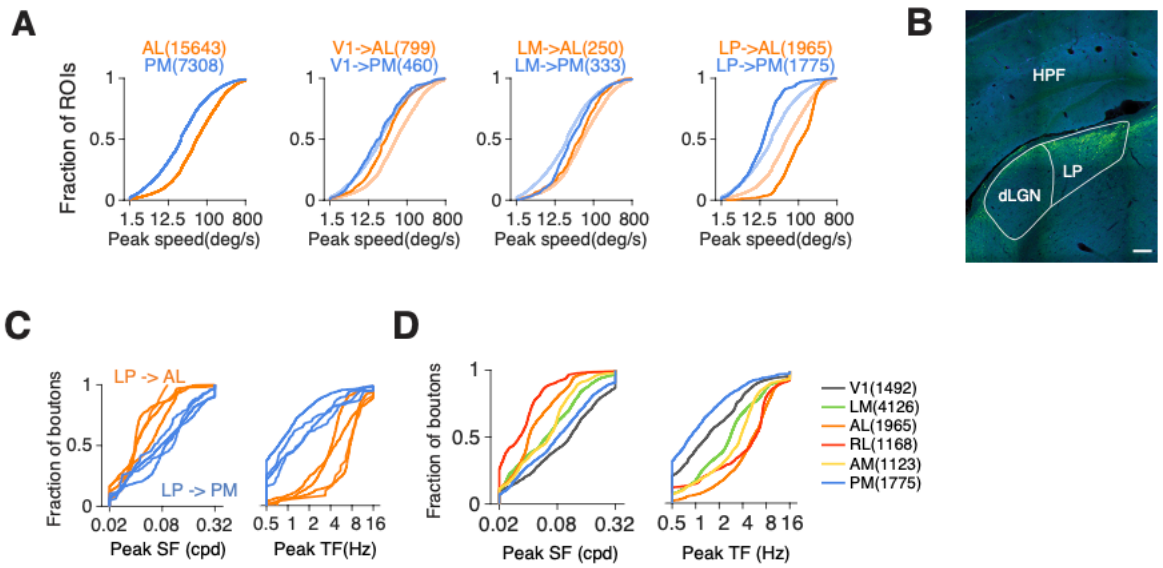

Figure S7. LP conveys specific information to higher visual areas, related to Figure 7.

(A) Cumulative distributions of peak speeds of (from left to right) neurons in AL or PM, AL-projecting and PM-projecting neurons in V1, in LM, and LP axons.

(B) Example image of GCaMP6 expression after stereotaxic injection in LP.

(C) Cumulative distributions of peak spatial and temporal frequencies of LP axons projecting to AL or PM in different mice (four mice for each group).

(D) Cumulative distributions of peak spatial and temporal frequencies of LP axons projecting to different cortical areas.